The Pennsylvania State University

The Graduate School

Department of Mechanical and Nuclear Engineering

HEAT TRANSFER AND PRESSURE DROP AUGMENTATION IN MICRO CHANNELS WITH PIN FINS

A Thesis in

Mechanical Engineering

by

Stephen A. Weaver

Submitted in Partial Fulfillment
of the Requirements
for the Degree of

Master of Science

May 2010

The thesis of Stephen A. Weaver has been reviewed and approved* by the following:

Karen A. Thole
Head of the Department of Mechanical and Nuclear Engineering
Professor of Mechanical Engineering
Thesis Advisor

H. Joseph Sommer III
Professor-In-Charge of MNE Graduate Programs

Laura L. Pauley
Professor of Mechanical Engineering

*Signatures on file in the Graduate School.

ABSTRACT

Since increased turbine inlet temperatures provide higher turbine efficiencies, gas turbine designs have progressed to the point where inlet temperatures are higher than the melting point of the airfoil materials. To ensure turbine airfoils do not melt during operation, complex internal and external cooling schemes are employed. Internal cooling methods have progressed from simple smooth walled channels that route cooling air through the airfoil, to designs with channels containing pin fins or rib features that serve to increase the channel surface area and the heat transfer coefficient by imparting turbulence to the flow.

To augment the performance of the main internal cooling channels, micro channels on the order of 0.5 mm can be placed within the airfoil walls between the hot external blade surface and internal main cooling channel. Being located adjacent to the external airfoil surfaces, the micro channels can efficiently cool the blade with a low thermal resistance to the hot outer surface. In previous studies, the effects of channel features have been mostly studied at large scales where discreet cooling features can be observed for Reynolds numbers matched to realistic turbine applications. For micro channels, there is concern if the correlations derived from these large scale experiments can be used due to the inherent surface roughness and manufacturing tolerances at such small scales.

In addition to surface roughness concerns, gas turbines operating in sandy environments can ingest significant amounts of sand that can deposit on airfoil internal channels and adversely raise the overall pressure drop and lower the flow available to cool the airfoil micro channels. The quantitative effects have yet to be studied for micro channel geometries and it is hypothesized that at the micro channel scales, sand ingestion could have a significant effect on reducing the channel cooling.

This thesis contains two papers that document the relevant work to determine how well correlations derived from large scale tests can predict the cooling for actual manufactured micro channels. The first paper focused on developing a testing methodology to accurately measure overall heat transfer and pressure drop for micro channel coupons with random roughness levels that would occur in turbine airfoils. Various coupons were fabricated with levels of surface roughness equal to the resulting roughness from typical casting techniques. The measurements showed that the surface roughness has an effect on the heat transfer augmentation when the

roughness approaches 2.2% of the channel height, yet augmentation in pressure drop occurs when the roughness level approaches 1.0% of the channel height.

The second paper focused on determining if correlations developed from large scale experiments with pin fin arrays can be used for micro channels having the same non-dimensional geometric features. Various micro channels with pin fin arrays were manufactured by the project sponsor and were then characterized in terms of heat transfer and pressure drop augmentation. In addition, these tests were done before and after room and engine temperature sand injection to characterize the effect of sand ingestion. The micro channel heat transfer and friction factor data matched correlations developed from large scale experiments over the range of Reynolds numbers tested. Room temperature sand ingestion at low pressure ratios decreased the amount of coolant flow through the channel. However, at pressure ratios above 1.4, the effects of sand ingestion were diminished as the higher velocity air forced the sand completely through the channel. Heated sand ingestion had a cumulative effect of lowering air flow at a fixed pressure ratio, along with lowering the channel heat transfer resulting from the sand adhering to the channel surfaces.

TABLE OF CONTENTS

List of Tables

List of Figures

Preface

This thesis contains two papers organized in manuscript format. The first paper, titled "Micro Channels with Manufacturing Roughness Levels," presents the design and development of a testing methodology to measure the heat transfer coefficient and pressure drop of gas turbine airfoil micro channels. The paper presents the uncertainty analysis that drove the development of the test chambers and the baseline comparison against published literature results. In addition, the paper describes the micro channel heat transfer and pressure drop effect of representative manufacturing surface roughness levels. This paper was accepted to the 2010 ASME Turbo Expo in Glasgow, Scotland along with being recommended for publication in the *Journal of Turbomachinery*.

The second paper, titled "Comparison of Micro Channels Containing Pin Fin Arrays with Available Correlations of Heat Transfer and Pressure Drop Geometries," presents the results of an experimental program to determine if pin fin turbulated channel heat transfer and pressure drop correlations derived at large scale can be used in the design of micro channels. Additionally, the effects of room temperature and heated sand ingestion on channel performance were studied. Micro channel heat transfer coefficients and pressure drops were measured for various pin fin arrays before and after sand injection. This paper will be submitted to a future ASME Turbo Expo.

Acknowledgements

After seven years in college, over two universities and two states, there are so many people to thank who made it all possible. First, I would like to thank my parents who were always there for me whether I was ten minutes down the road at NC State or ten hours away at Penn State. Every time I called, they would always put me in better moods. The random packages of cookies and goodies also helped. They always kept me on the right track; who knows where I would be without them. I would also like to thank them and my grandparents for paying for me to go through school. I never would have had the opportunity to come back and get my Masters if they had not giving me the means to pay for my education.

At Penn State, I would like to thank my advisor Karen who has guided me to the Engineer I am today. Every Monday she always had a smile on her face, ready to work though all the problems I had the previous week. I would also like to thank my lab mates: Grant, Gaelyn, Jason, Steve, Seth, Alan, Gina, Nick, Robert, and Dwayne. I will always remember the late nights, weekends, and fun times whether they were downtown or working around the lab. And especially Mike, you always had an answer whether I had a rookie question or needed a helping hand. Lastly, thank you to Pratt & Whitney for giving me the opportunity to work with them and in helping guide me through the semesters.

I would also like to thank my friends at NC State, Penn State and in-between. I will never forget the good times over my years in college and my first years in the real world. Lastly, thanks to my sister Katie for all the fun times over the past 26 years.

Paper 1: Micro Channels with Manufacturing Roughness Levels

Recommended to *Journal of Turbomachinery* (2010)*

Abstract

There are heat transfer advantages to reducing the size of channels used for internal cooling gas turbine components. As channel sizes decrease, however, there are concerns as to how manufacturing surface roughness may affect the channels expected pressure drop and heat transfer. For micro channel size scales, in particular, there is relatively little data indicating the effect of manufacturing roughness levels.

The focus of this paper is to describe the development and validation of a testing method for micro channels as well as determine the effect of manufacturing roughness levels on these small channels. Convective heat transfer coefficients and friction factors were deduced based on measured flow conditions and known boundary conditions. It was shown that at an average roughness height of 6.1 μm, which corresponded to 2.2% of the channel height, heat transfer was augmented by 1.1 - 1.2 while the friction factor was augmented significantly more by 2.1 - 2.6 over a smooth channel.

Nomenclature

A	area
C_p	specific heat
D_H	hydraulic diameter: $D_H = \frac{2(W \cdot H)}{(W+H)}$
f	friction factor: $f = \frac{\Delta P}{0.5\left(\rho_i \cdot V_i^2\right)} \frac{D_H}{L}$
h	heat transfer coefficient
H	micro channel height
k	thermal conductivity
K	loss coefficient
L	channel length
$\dot{m}$	mass flow rate
Nu	Nusselt number: $Nu = \frac{h \cdot D_H}{k_{air}}$

*Weaver, S.A., Barringer, M.D., and Thole, K.A., 2010, "Micro Channels with Manufacturing Roughness Levels," ASME Paper No. GT2010-22976.

P	pressure
ΔP	pressure difference
ΔP_t	total pressure difference
Q_H	power from heaters
Q_L	energy loss
Q_{net}	net convective heat transfer
R	gas constant
R_a	average surface roughness
R_z	maximum surface roughness
Re	Reynolds number: $Re = \frac{\rho \cdot V \cdot D_H}{\mu}$
ΔT_{LM}	log-mean temperature difference: $\Delta T_{LM} \frac{(T_s - T_o) - (T_s - T_i)}{\ln\left(\frac{T_s - T_o}{T_s - T_i}\right)}$
T	temperature
V	velocity
W	channel width
x	transverse distance from channel center
y	vertical distance from channel center
z	horizontal distance from channel inlet

Greek:

ρ	density
μ	dynamic viscosity

Subscripts:

c	coupon
cu	copper
i	inlet
int	copper and coupon interface
o	outlet
s	surface

Introduction

As turbine operating temperatures continue to rise, there is the ever present problem of cooling airfoil components. To accomplish this, cooling methods have morphed into a complex array of specialized internal and external schemes. A majority of cooling methods involve routing cool air from the compressor, through internal cooling channels and out through various film cooling holes around the blade surface. These cooling channels serve as a means to transfer

heat from the airfoil surfaces to a cooling flow passing through the inside of the vanes and blades.

Internal cooling has evolved from simple smooth-walled channels, to ones that include various types of features that serve to increase the convective heat transfer coefficient and heat transfer surface area. Internal cooling features have been studied in detail over the years and the most preferred cooling designs involve pin fins, ribs, and various surface roughening effects such as dimples. They serve to increase the turbulent mixing of the flow as it passes through the channel, thereby increasing the convective heat transfer coefficient along the wall surfaces.

There are many advantages from a cooling perspective to use micro channels to cool components, provided the pressure to drive the flow through these channels is available. These micro channels approach the level where manufacturing (random) roughness and tolerances can play a key role in their heat transfer capabilities [1]. Average manufacturing roughness in common casting techniques can approach 1 - 10 μm [2] before polishing or finishing, and this seemly inconsequential inherent roughness can discernibly affect the micro channels' heat transfer and pressure drop.

This paper provides a summary of the findings of an experimental program focused on examining the heat transfer and pressure drop of micro channels. Accurately quantifying these two parameters will enable better prediction of the engine hardware thermal performance and life. The primary objective of this study was to develop a testing procedure capable of evaluating the heat transfer and pressure drop performance of several micro channels over a range of Reynolds numbers. The performance is reported in the form of an overall Nusselt number and friction factor for each manufacturing roughness level. While the results indicate little dependence of heat transfer and pressure drop augmentation upon Reynolds number, the range studied was in the fully turbulent regime in which compressibility effects were not present.

Relevant Past Studies

Micro channel cooling has only recently been studied in the gas turbine field. The main benefit from this method is that it provides minimal conductive thermal resistance between the cooling fluid and the external hot gases. However, micro channel cooling with surface roughness, has been studied extensively for channel heights in the sub 500 μm range by the biomedical, electronics, and cryogenic cooling fields and in the large scale range (> 10 mm) by

the heating, ventilating, and air conditioning (HVAC) and energy fields [3, 4]. Very little data exists in the micro channel range between these two sizes, and yet the between range is the most applicable to the gas turbine fields.

The biomedical, electronics, and cryogenic cooling fields have focused on using single and two-phase flow, liquid nitrogen, and other refrigerants having micro channel dimensions on the order of 20 - 500 μm [5, 6]. The studies in these fields predominately focused on the laminar and transitional regimens, and do not report data expansively into the fully turbulent regime.

Qi et al. [7] studied the effect of surface roughness on the cooling performance of liquid nitrogen in micro channels with diameters of 0.5 mm to 2 mm over a wider range of Reynolds numbers. Over a Reynolds number range of $1x10^4$ - $9x10^4$, they found that roughness increased the heat transfer and pressure drop over a smooth channel, but the pressure drop augmentation was less at higher temperatures due to lower nitrogen viscosities.

In the sub 500 μm range, little data exists on gas cooled channels in the fully turbulent regime. Lorenzini et al. [8] studied nitrogen gas to cool circular micro channels with diameters of 25 μm - 508 μm. They found that at low Reynolds numbers in the laminar regime, their results accurately matched the literature results. However, when fully turbulent, the results deviated due to compressibility effects. Their reported data was in the fully turbulent regime, but stopped at a Reynolds number of $1x10^4$.

One of the first studies of micro channel heat transfer in the gas turbine field was performed by Marques et al. [9], where a pin fin micro heat exchanger was developed having channels with a height of 0.5 mm that contained various pin arrays. The arrays had a height to diameter ratio of one and a staggered spacing to diameter ratio of 2.5. Over a Reynolds number range of $4x10^3$ - $2x10^4$, the array augmented heat transfer on the order of 4 - 5 and friction factor on the order of 15 - 20, over a smooth channel.

Bunker et al. [10] studied various types of arrays of round and diamond pins, and pins with various wall dimple configurations in small channels. He tested channel widths of 33 cm and heights of 5.08 mm, which gave an aspect ratio of 65:1 (W:H). Tests were conducted with round pin fin axial spacing to diameter ratios of 1.5 and height to diameter ratios of 0.2, which differs from usual array height to diameter ratios of greater than one. Bunker's findings indicated the dense arrays augmented the heat transfer by approximately 2.25 times over a

smooth channel. The arrays with pins and dimples performed better, augmenting the heat transfer by more than 3, but at a friction factor augmentation of up to 25.

Bunker [11] also studied the use of small pin fins in mesh-fed film cooling. The aim was to increase the film effectiveness downstream of a slot by placing small pin fin arrays immediately upstream of the slot flow exit. The pin height to diameter ratio was 0.2, with slot blowing ratios of 0.1 - 0.7. The results were that the coolant stream did not blow off the wall, even at the higher blowing ratios where this would be expected. Cooling was augmented by 25 - 100% in the downstream section when compared to cooling without the arrays.

As internal channels approach smaller and smaller dimensions, such as those being studied in this experiment, manufacturing tolerances can also play a role in the overall heat transfer performance of the channels. Bunker [1] performed a review on the effects of various tolerances on the cooling performance of channels that included film cooling, impingement cooling, internal cooling passages, and turbulated channels. The study concluded that channel geometry tolerances affected the heat transfer by 1%, but manufacturing tolerances for channel features affected the heat transfer even more by 2 - 7%.

This paper presents a method for discerning manufacturing roughness effects on heat transfer and pressure drop for micro channels that fall between the sub 500 μm and large scale (> 10 mm) ranges, which is relevant to gas turbine engines. The remainder of the paper presents the design and validation of the testing apparatus, followed by results of measured pressure drop and heat transfer for a number of coupons.

Experimental Apparatus

A test stand and individual chambers were designed to test micro channel coupons and minimize the overall uncertainty of the heat transfer and pressure drop measurements. The overall apparatus is shown in Figure 1.1. The primary components of the stand included a high pressure air supply line with regulator valve, a primary test chamber, and a downstream exhaust line with regulator valve. Compressed air was supplied to the test stand at 22°C and 450 - 620 kPa gauge, and the flow rate was measured using a laminar flow element located upstream of the test chamber. The high pressure air then passed into the test chamber and subsequently out through the second regulator valve, which was used to adjust the downstream pressure and flow rate through the chamber. Two test chambers were constructed: one for measuring heat transfer

and one for measuring pressure drop. These two chambers were designed to be easily interchanged and to share the maximum common instruments between the two.

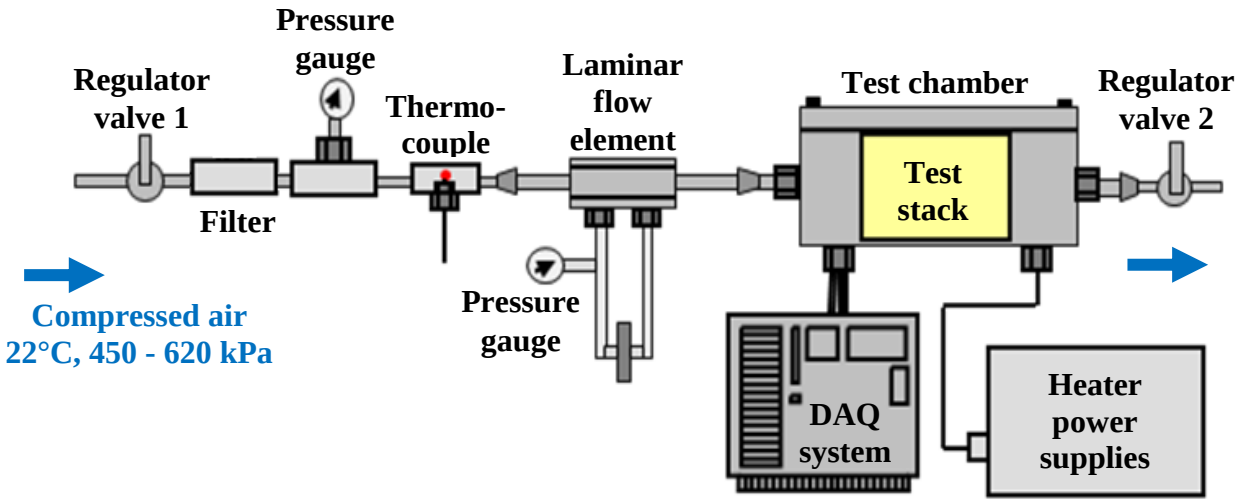

Figure 1.1. Schematic of the micro channel test apparatus designed in this study.

An axial cross-section of the heat transfer test chamber is shown in Figure 1.2. The outer enclosure of the test chamber was fabricated from a hard plastic known as polyetheretherketone (PEEK) having 1.6 cm thick walls. This material was selected due to its low thermal conductivity as shown in Table 1.1, high tensile strength, and good machining properties. A low thermally conductive material was necessary to minimize the heat loss from the test chamber to the surrounding atmosphere, while the high tensile strength was desirable due to the elevated operating air pressure within the test chamber. The PEEK test chamber contained a sandwich of pieces that included a stack of rigid foam insulation, copper heat sinks, electric circuit heaters, and the coupon. Axially centering the stack gave identical reservoirs upstream and downstream to allow measurement of the inlet and outlet pressure and temperature of the air.

The foam was rigid polyurethane and was selected due to its low thermal conductivity (as shown in Table 1.1) in combination with its other desirable characteristics including a wide temperature use range and high compressive strength.

Photographs of the test section construction are shown in Figure 1.3. The foam was used as an insulator around the coupon and copper heat sinks. The insulation reduced the heat loss from the heaters to approximately 2 - 4% for the range of Reynolds numbers tested. To ease the transition from the large upstream reservoir to the small coupon channel, a trapezoidal inlet was

built into the foam insulation. Downstream of the coupon where the outlet air temperatures were measured, the channel had a constant cross-section.

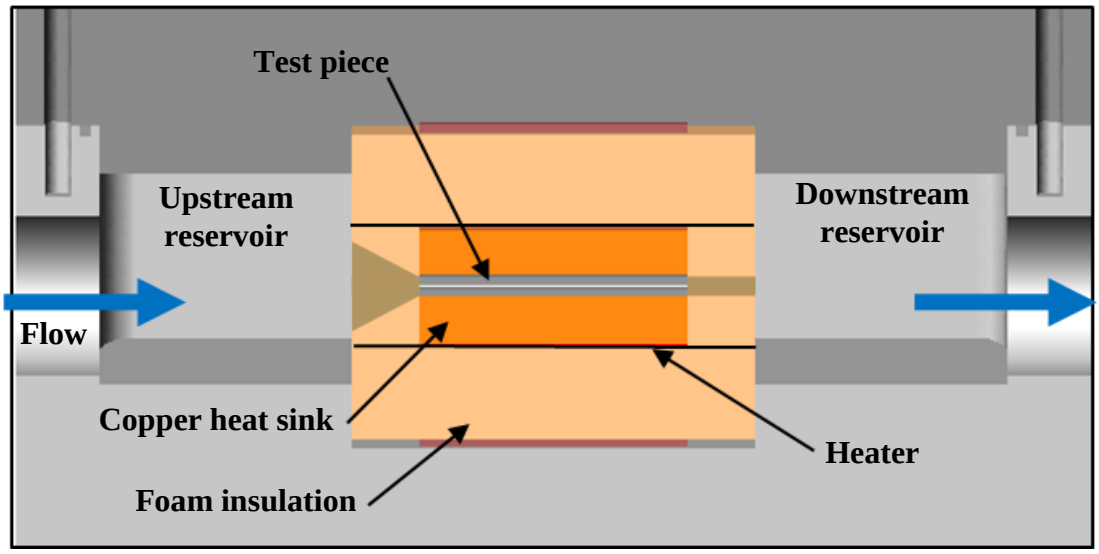

Figure 1.2. Axial view of the heat transfer chamber and internal components.

Table 1.1. Test Chamber Thermal Properties

Material	k (W/m K)
PEEK	0.25
Copper	400
Foam	0.054
Conductive Paste	2.31

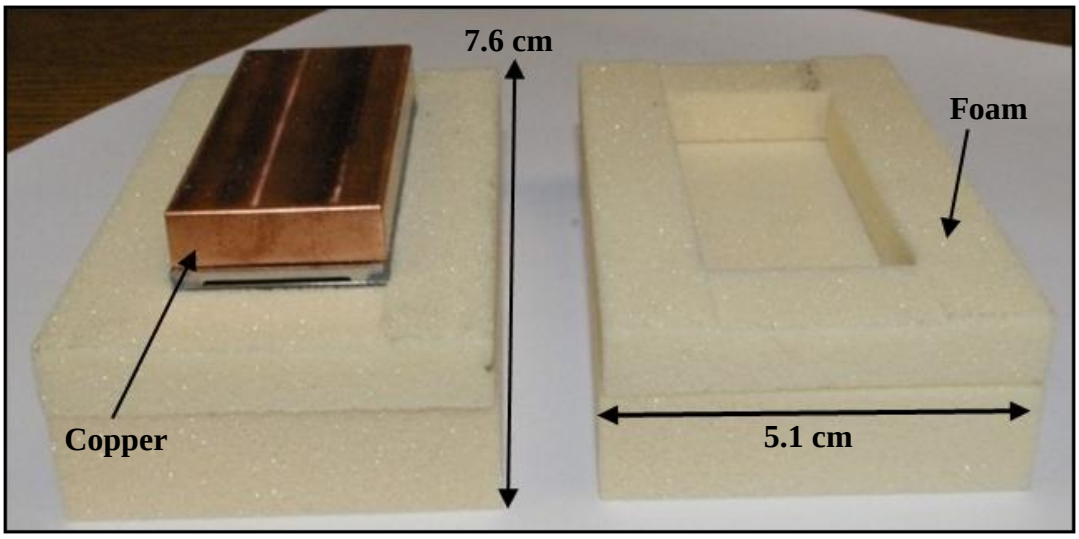

Figure 1.3. Photograph of the foam insulation used to surround the coupon and heat sinks.

The copper blocks were heated using two identical circuit heaters positioned between the copper and the surrounding foam insulation. The heaters were chosen for their ability to provide a constant heat flux boundary condition to the surface of the copper of up to 12.3 W/cm^2. Since copper has a very high thermal conductivity (as shown in Table 1.1), the constant heat flux being supplied by the heaters resulted in a copper heat sink that was nearly spatially uniform in temperature, as verified later in this study through numerical simulations. This uniform copper temperature was then the physical boundary condition for the coupon.

To ensure all of the flow passed through the coupon channel (and not around it through the foam stack), all upstream interfaces were sealed with a silicone sealant. In addition, all downstream edges were sealed using high vacuum grease.

The test chamber used to quantify pressure drop differed in the fact that there were no heaters or insulating materials needed, as shown in Figure 1.4. This test chamber was manufactured to have an upstream chamber to decelerate the flow to measure a total upstream pressure, a nozzle inlet to the coupon, and a downstream chamber to measure total downstream pressure. The inlet nozzle was designed to reduce any entrance losses. The downstream reservoir provided the same benefit as in the heat transfer chamber, which was to provide a fixed back pressure to remain at low Mach numbers (< 0.2) through the channel. The supply air pressure was kept at a constant pressure and the downstream pressure was throttled with the regulator valve. The coupon was attached to the nozzle wall using a compression fitting with a notch cut into it as to not impede the exiting flow.

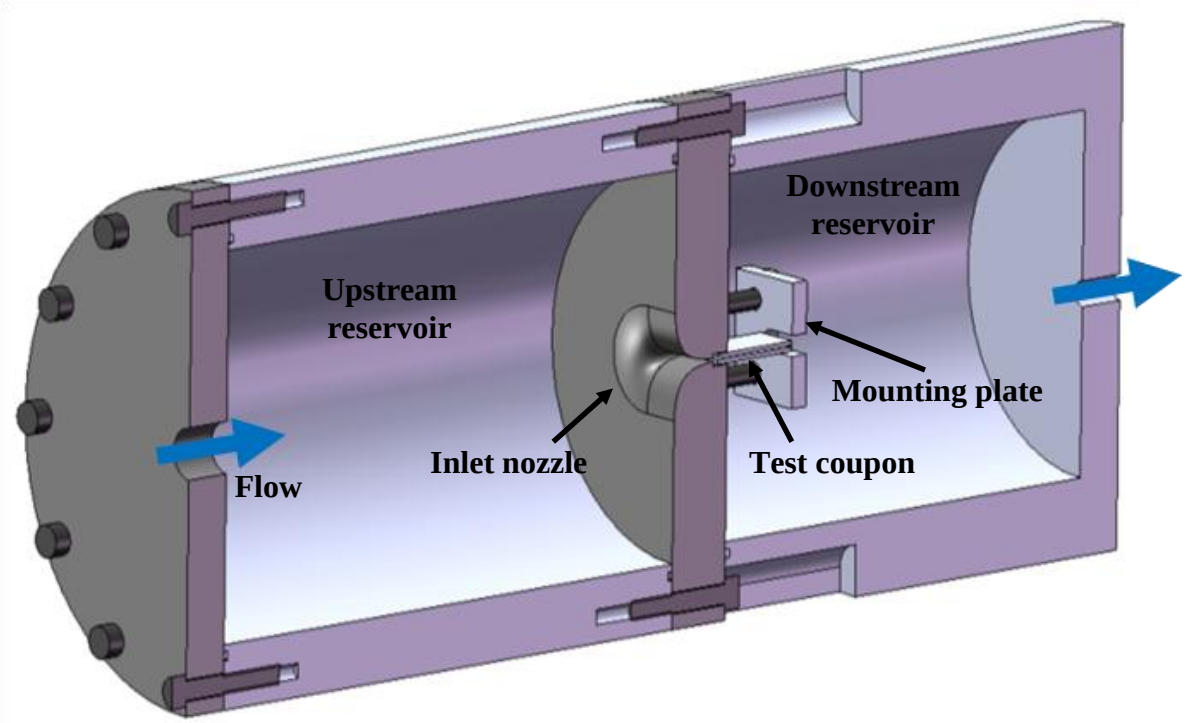

Figure 1.4. Axial view of the pressure drop test chamber and internal components.

Instrumentation

For the heat transfer tests, the entire test apparatus including the primary PEEK test chamber and upstream delivery pipe were instrumented to ensure measurement redundancies and minimize uncertainties. Figure 1.5 shows the locations in which temperature and pressure measurements were taken. All temperature measurements were performed using type-E thermocouples, with multiple temperature measurements made to verify an even temperature distribution across the pitch direction.

The copper heat sinks were each machined with six evenly spaced insertion holes that allowed the installation of thermocouples at the mid-plane of the heat sinks. Each insertion hole was filled with a highly thermally conductive paste (as shown in Table 1.1). As with the copper blocks, temperature measurements were taken upstream and downstream of the coupon in the foam blocks. Six evenly spaced thermocouples were also positioned in the top and bottom foam pieces to calculate the amount of heat loss from the test chamber.

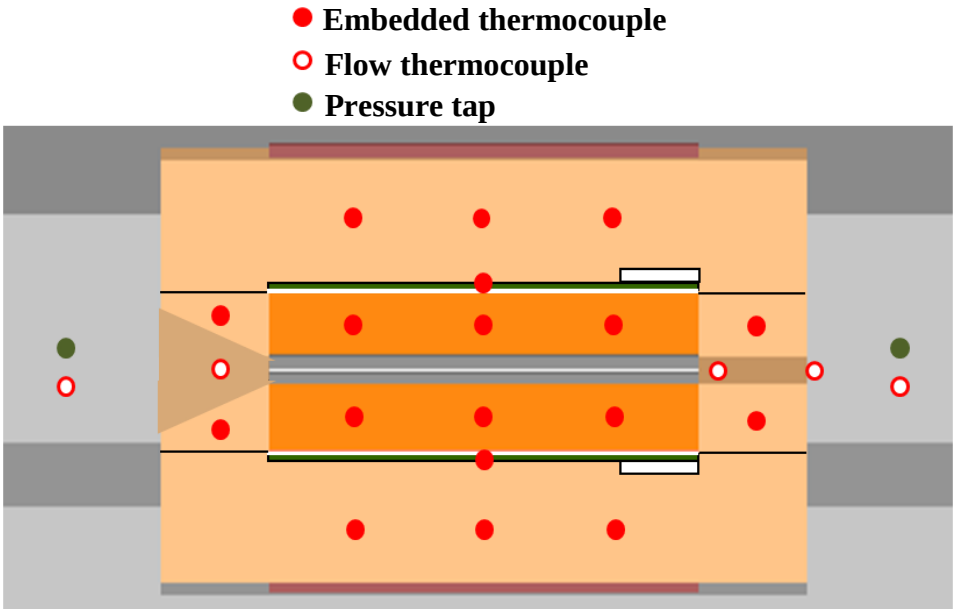

Figure 1.5. Drawing of measurement locations within the test apparatus.

Figure 1.6 shows examples of the thermocouples installed within the test stack that measured the coupon outlet air temperature. Four thermocouples were placed at the exit of the coupon and four were placed at the exit of the foam. These two streamwise locations were used to provide two measurement points for accurately measuring the outlet temperature. The foam exit was used as the outlet location for calculating the overall heat transfer coefficient.

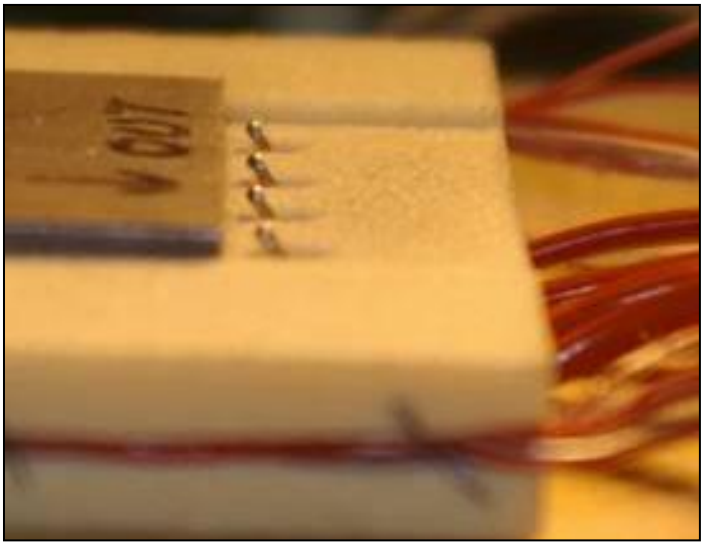

Figure 1.6. Photograph of thermocouples installed at channel exit.

As for the pressure drop test chamber, pressure measurements were made in the upstream and downstream chambers, and across the chambers. The individual pressures were used to

calculate the air densities, while the differential measurement across the chambers provided an accurate measurement of the total pressure drop.

Description of Micro Channel Coupon

Four coupons were manufactured for testing the effect of random manufacturing roughness in micro channels. They were fabricated out of a proprietary metal that had a high thermal conductivity relative to the insulating materials. To minimize the thermal resistance between the heaters and the copper blocks, as well as between the copper blocks and the coupons, a thin layer (0.08 mm) of thermally conductive paste was applied across the outer surface of the coupon (properties shown in Table 1.1).

To fabricate a micro channel with a specified surface roughness, the coupons had to be manufactured in two separate parts and then attached as seen in Figure 1.7. The top and bottom pieces were fabricated using wire or plunge electric discharge machining that provided a specified surface roughness, and then attached using a thermally conductive cold-weld on the streamwise sides of the pieces. Each coupon had an internal channel width of 17.8 mm and height of approximately 500 μm, which was measured using high accuracy pin gauges. The coupons had an overall width of 2.5 cm and length of 5.0 cm.

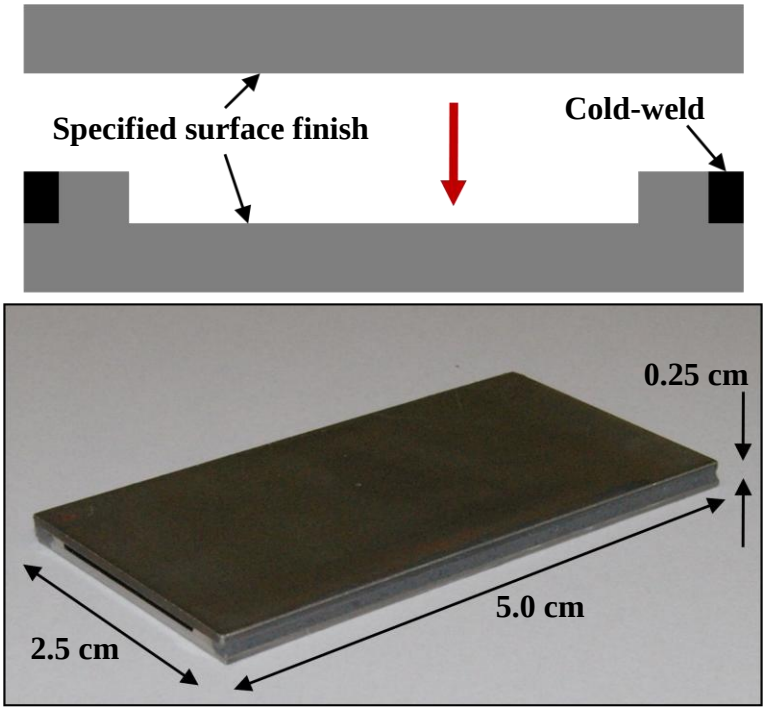

Figure 1.7. Diagram of coupon assembly process and overall dimensions.

The parameters of the four coupons tested are shown in Table 1.2 which includes the following: manufacturing method, average surface roughness (R_a), maximum surface roughness (R_z), and channel height (H). The average roughness was defined as the average of the differences between a roughness height and roughness mean across the sample, while the maximum roughness range was the average of the ten largest differences between peaks and valleys [12]. The average and maximum surface roughness are described as a 95% confidence interval of the data measured on the top and bottom surfaces. The channel height is the height measured using the pin gauges plus $4R_a$, with an uncertainty calculated using the partial derivative method by Kline and McClintock [13]. Figure 1.8 shows a sample of a three-dimensional surface plot of coupon MR3, taken using an optical profilometer. The random roughness is noticeable with various peaks and valleys across the surface.

Table 1.2. Coupon Roughness Properties

Coupon	H (µm)	Manufacturing Method	R_a (µm)	R_z (µm)
Smooth	508.6 ± 2.6	Wire-EDM and polished	0.14 ± 0.06	3.2 ± 0.9
MR1	505.6 ± 2.6	Wire-EDM	2.6 ± 0.2	26.2 ± 2.2
MR2	525.6 ± 3.2	Plunge-EDM	4.4 ± 0.6	38.4 ± 6.4
MR3	557.8 ± 5.9	Plunge-EDM	6.1 ± 1.7	46.2 ± 9.6

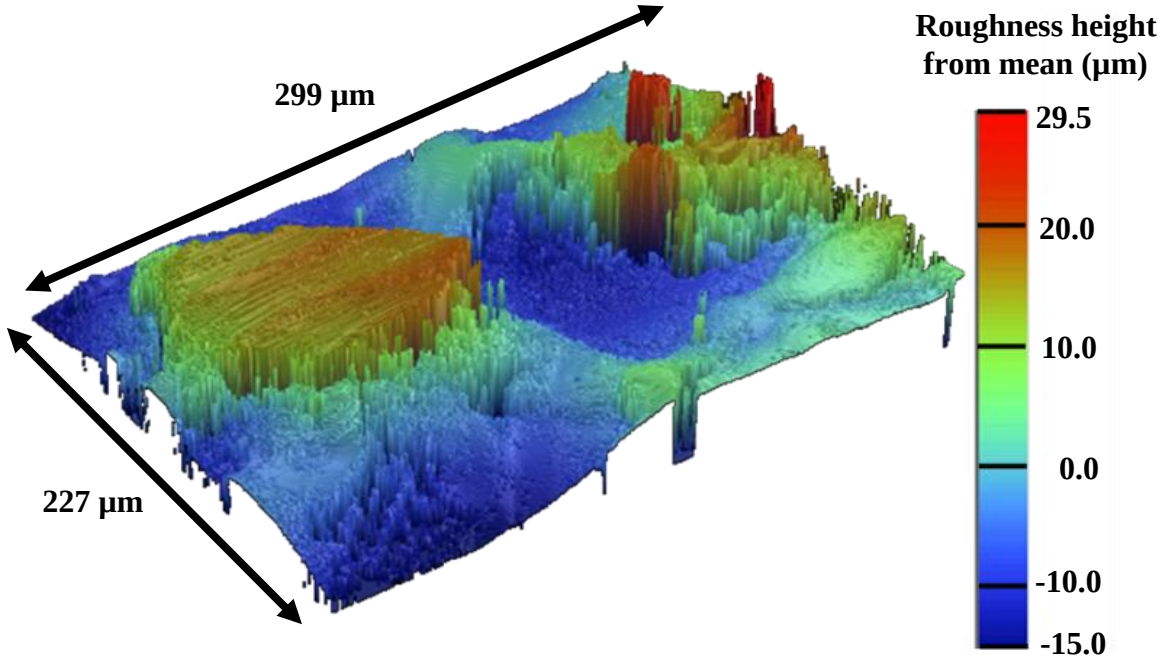

Figure 1.8. Coupon C three-dimensional profilometry surface plot.

Test Method and Data Reduction

The overall convective heat transfer coefficient for each coupon was determined by using Equation 1.1 and verified using a first law energy balance (Equation 1.2).

$$Q_{net} = h \cdot A_s \cdot \Delta T_{LM} \tag{1.1}$$

$$Q_{net} = \dot{m} \cdot C_p (T_o - T_i) \tag{1.2}$$

The symbol ΔT_{LM} was the log-mean temperature difference between the flow and the micro channel walls. In Equation 1.2, the net convective heat transfer was given by $Q_{net} = Q_H - Q_L$. The justification of using ΔT_{LM} was based on the assumption that the wall temperature remained uniform through the streamwise and spanwise dimensions, and was verified using numerical simulations as discussed below.

Due to the small physical size of the micro channels, the internal wall temperature could not be directly measured in this study and was instead modeled using a one-dimensional analysis. The channel wall temperature, Equation 1.3, was calculated using a thermal resistance network from the measured temperature of the copper heat sinks to the channel wall.

$$T_s = T_{cu} - \left(0.5 \cdot \Delta y_{cu}\right)\left(\frac{Q_{net}}{k_{cu} \cdot A_{cu}}\right) - \left(\Delta y_c\right)\left(\frac{Q_{net}}{k_c \cdot A_c}\right) \tag{1.3}$$

Between the measured copper temperature and the wall temperature were two thermal resistances from the copper thickness and coupon wall thickness, which is shown in Figure 1.9. The temperature drop through the thermally conductive paste was negligible due to the minimal thickness and high conductivity.

To determine the overall friction factor of the micro channels, the density and velocity were defined using channel inlet conditions. In this experiment, ΔP was defined as the difference in measured total pressures between the upstream and downstream reservoirs and then modified for the sharp expansion loss at the exit as shown in Equation 1.4. For a sharp exit into a large reservoir, the value of K was accepted as 1.0 [14]. By designing a smooth nozzle between the upstream reservoir and the channel inlet, the inlet K value was assumed to be zero. Typical test flow conditions within the micro channels are summarized in Table 1.3.

$$f = \frac{\left[\Delta P_t - \frac{1}{2} K \rho_o V_o^2\right] \cdot D_H}{0.5\left(\rho_i \cdot V_i^2\right) \cdot L} \tag{1.4}$$

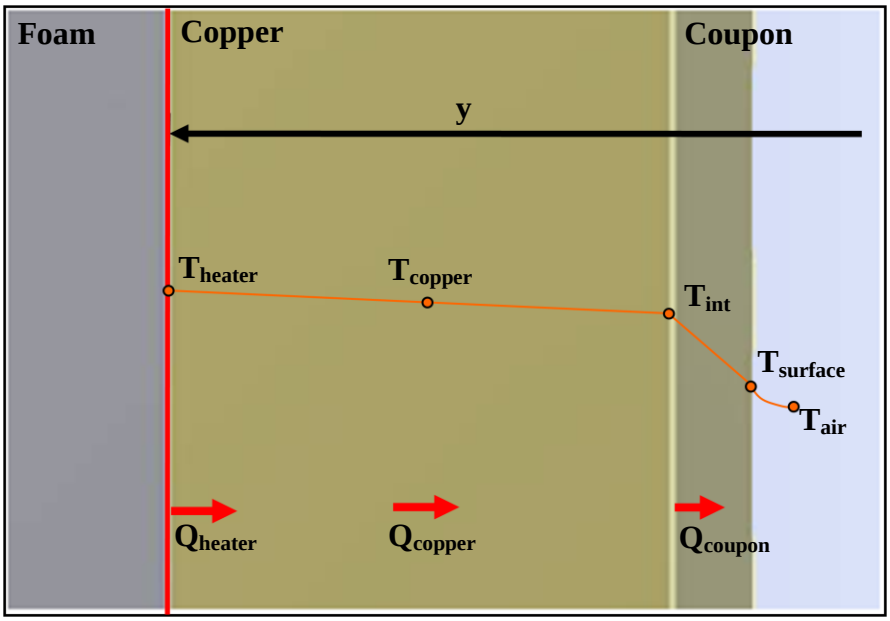

Figure 1.9. Schematic of a cross-sectional view of the test stack (foam to air).

Table 1.3. Typical Test Flow Conditions

Reynolds number, Re	$5x10^3 – 3.5x10^4$
P_i (kPa gauge)	450 - 620
T_s (°C)	38 - 93
$\dot{m}$ (kg/s)	0.001 – 0.005
Q_H (W)	38 – 110

Method Verification and Uncertainty

To determine the validity of the constant wall temperature assumption and resistance network calculation for the channel wall temperature (T_s), two-dimensional and three-dimensional steady state heat transfer simulations using the finite element computational software ANSYS 11.0 were performed. These simulations were carried out using the test flow conditions within the smooth coupon stated in Table 1.4.

Table 1.4. Numerical Simulation Parameters

Q_H (W)	106
Re	$2.4x10^4$
Nu	64

The two-dimensional simulation was performed to prove the validity of the one-dimensional resistance network assumption used to calculate T_s. This two-dimensional simulation at a streamwise mid-plane showed good copper temperature agreement with the one-dimensional resistance network.

A three-dimensional simulation was then performed using ANSYS 11.0 fluid link elements to determine the copper spatial temperature variation. The test stand was modeled with the same parameters as the previous two-dimensional simulation. Results indicated that the copper midpoint temperature varied by less than 2°C in the streamwise direction and by less than 1°C in the vertical direction when calculated at the channel mid-plane. This range was determined to be acceptable given the overall temperature rise of the fluid was 19 - 27°C for all tests.

Non-dimensional copper heat sink and coupon temperature contours are shown in Figure 1.10. T_i is the air temperature at the channel inlet and Q_{net} is the net convective heat transfer. This non-dimensional temperature is the ratio of the metal temperature rise to the overall air temperature rise through the channel. In addition, the horizontal copper mid-plane non-dimensional temperature is shown in Figure 1.11 and the vertical copper and coupon mid-plane non-dimensional temperatures at the channel inlet, midpoint, and outlet are shown in Figure 1.12 for the conditions shown in Table 1.4. Horizontal and vertical temperature locations are shown in Figure 1.10 as a dashed line.

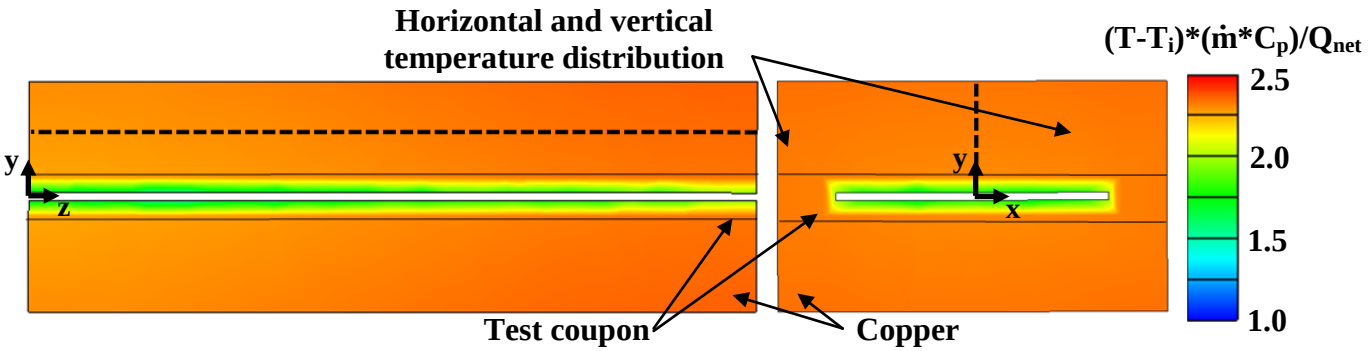

Figure 1.10. Three-dimensional ANSYS simulation of copper heat sinks and coupon temperatures.

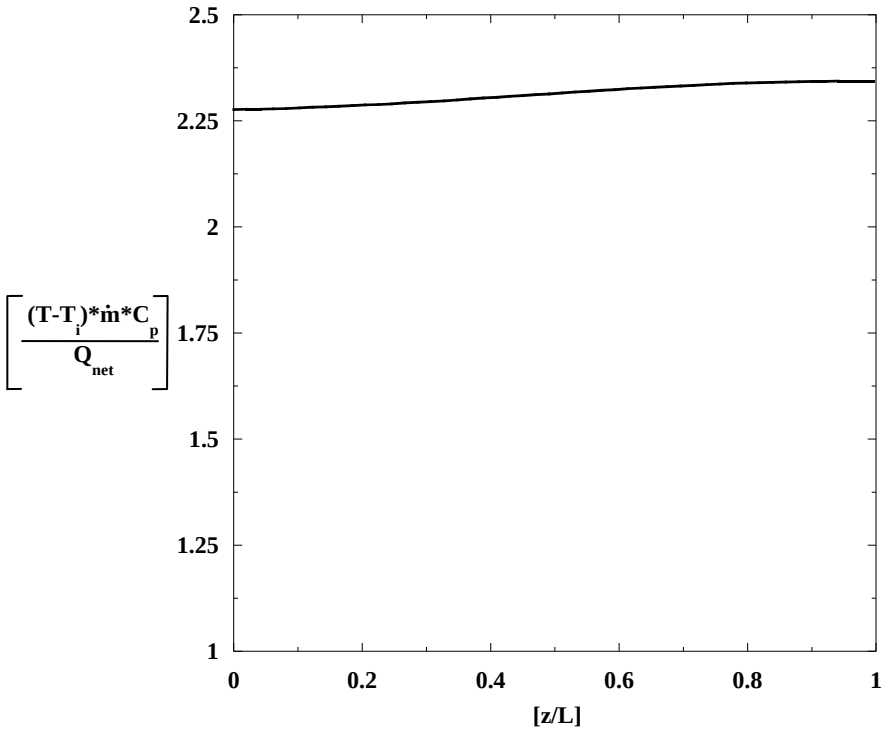

Figure 1.11. Copper mid-plane horizontal temperature distribution.

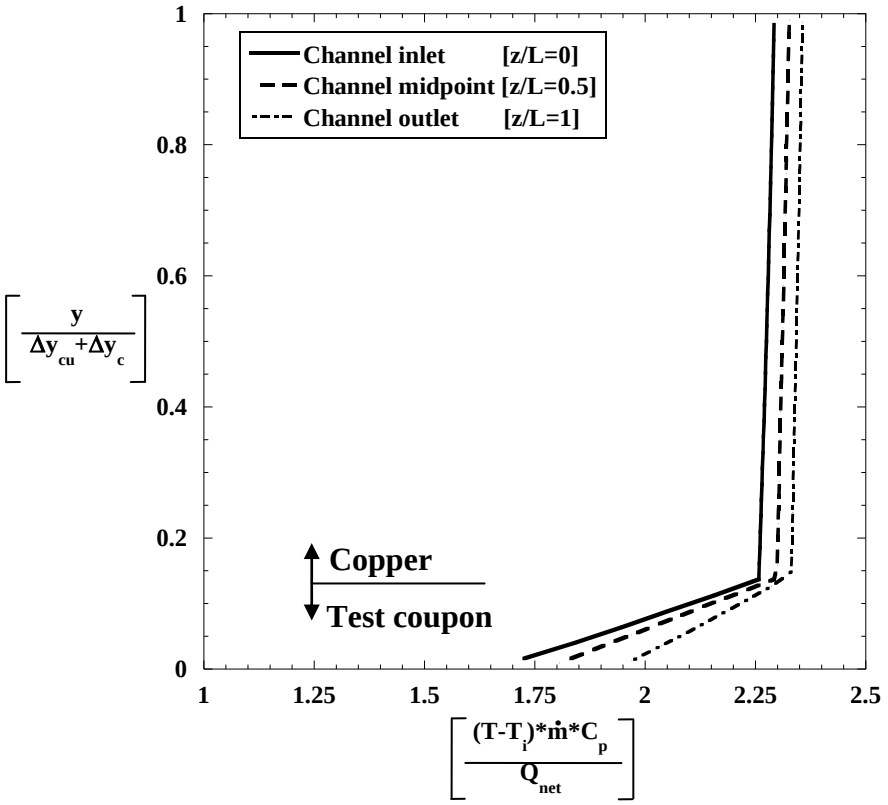

Figure 1.12. Copper and coupon mid-plane vertical temperature distribution.

To verify the heat transfer coefficients were measured accurately, a first law energy was checked as given in Equation 1.2. This check used the air temperature rise measured across the micro channel and mass flow rate to calculate the net amount of heat entering the air. The energy balance percentages, which represented the difference between the convective heat transfer measured using equation 1.2 and the convective heat transfer measured using $Q_H - Q_L$, are shown in Figure 1.13. For all coupons, the energy balances match what was expected from the heaters and were within ±8%.

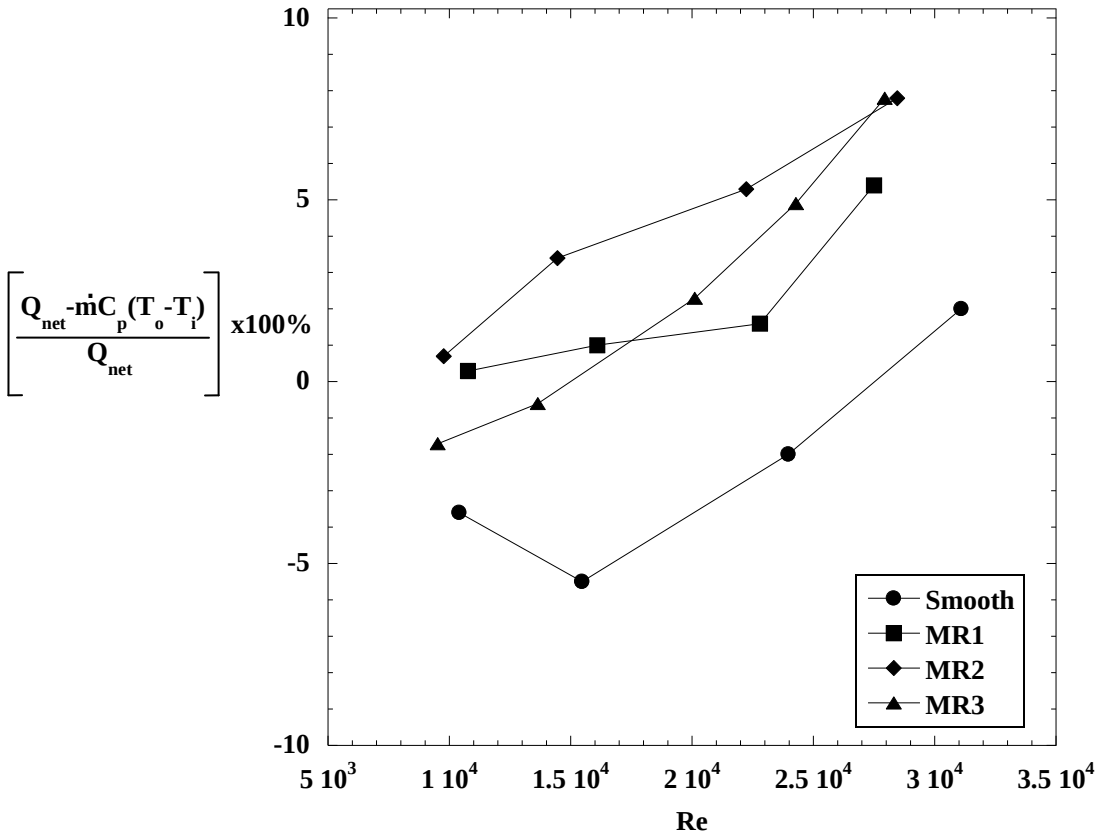

Figure 1.13. Coupon energy balance % as a function of Reynolds number.

An uncertainty analysis on the friction factor and convective heat transfer coefficient was performed using the partial derivative method described by Kline and McClintock [13]. To calculate the uncertainty of the convective heat transfer coefficient of the channel, twelve parameters were considered: heater individual and total power, channel surface area, copper temperature, copper thickness and coupon wall height, copper and coupon thermal conductivity, copper and coupon cross-sectional area normal to the heaters, and finally the air inlet and outlet

temperature. For a range of Reynolds numbers of $1x10^4$ - $3.1x10^4$, the uncertainty varies from 4.1 - 4.3%.

Figure 1.14 shows the percentage that each parameter contributes to the uncertainty, as a function of the total uncertainty to the convective heat transfer coefficient. The largest contributors to the uncertainty were the micro channel surface area (A_s), copper temperature (T_{cu}), and outlet air temperature (T_o). To reduce this uncertainty, as stated before, multiple temperature measurements were taken at each of the locations. This ensured an accurate average temperature and did not reduce these vital temperature measurements to a single point measurement.

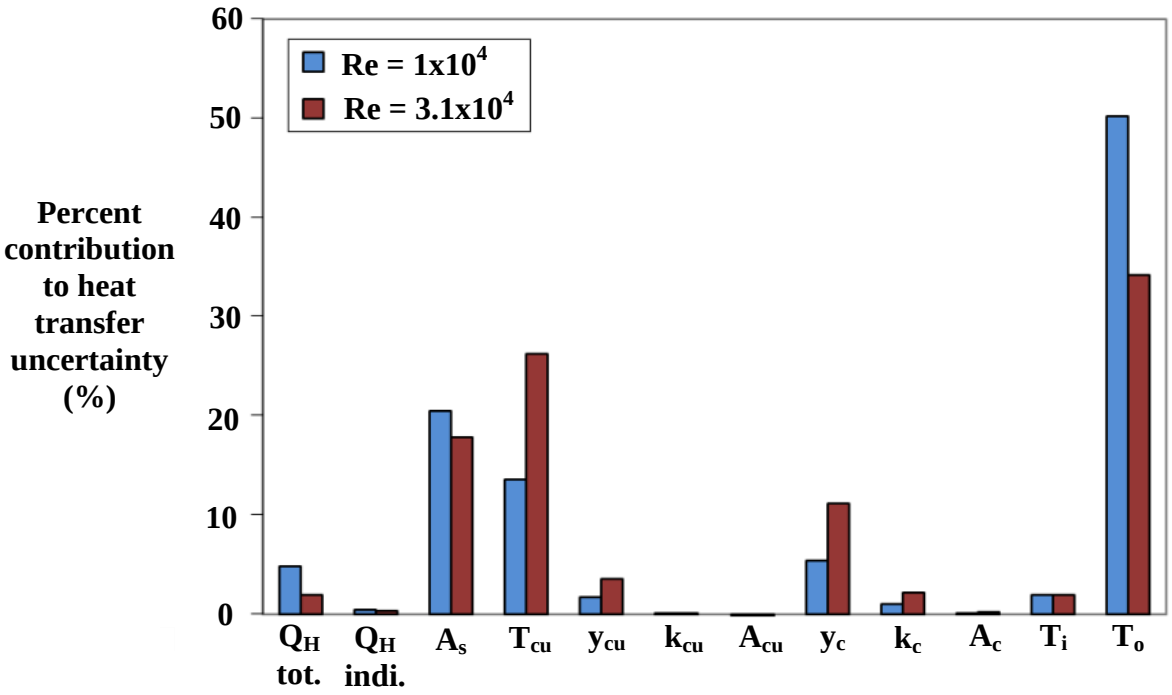

Figure 1.14. Individual parameter contributions to overall heat transfer coefficient uncertainty.

A similar analysis was performed for the friction factor chamber. Figure 1.15 shows the percentage that each parameter contributes to the uncertainty, as a function of the total uncertainty to friction factor. These parameters were: ΔP across the coupon, pressure of the upstream and downstream chambers, air temperature and gas constant, mass flow rate, and the channel height, length, and width. For a range of Reynolds numbers of $8x10^3$ - $3x10^4$, the uncertainty varies from 12.3 - 14.3%. Half of this uncertainty came from inaccuracies in

measuring the channel height. A small 0.01 mm uncertainty in channel height varied the channel area by 2%.

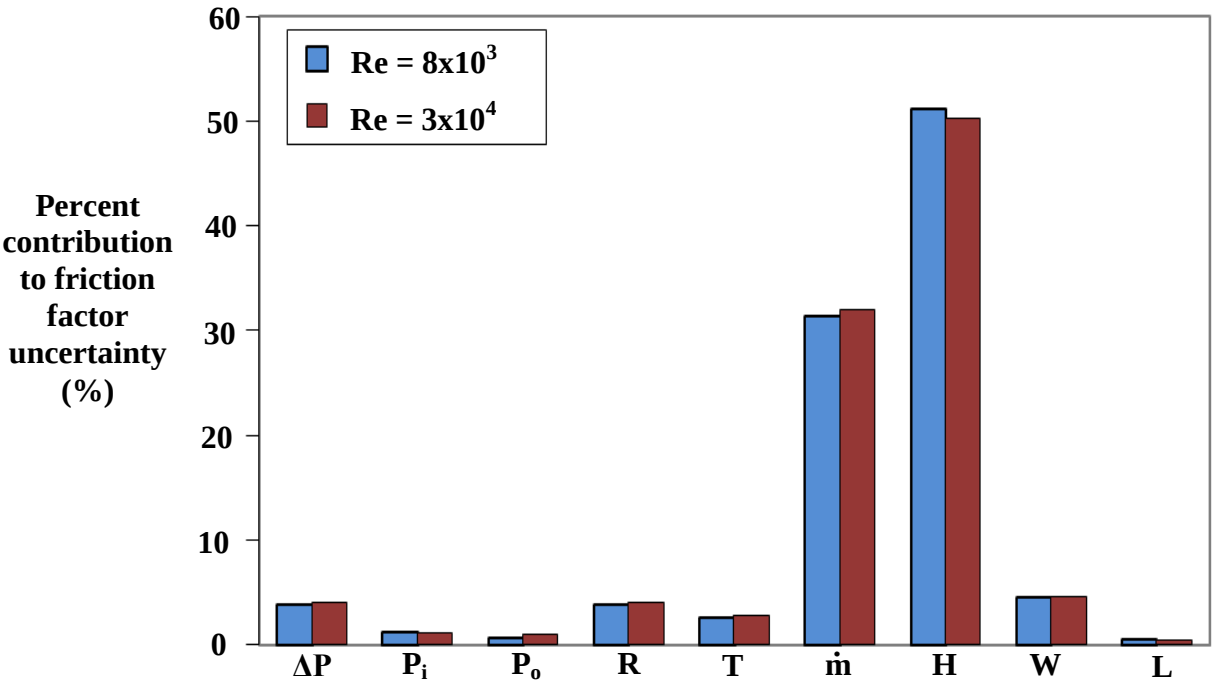

Figure 1.15. Individual parameter contributions to overall friction factor uncertainty.

Heat Transfer Test Results

Experimental results for heat transfer are shown below in Figure 1.16 and 1.17. Figure 1.16 also shows two correlations for smooth wall, fully-developed, turbulent internal channel flow. These correlations are the Dittus-Boelter correlation [15] as shown in Equation 1.5, and the Gnielinski correlation [15] shown in Equation 1.6. In the Gnielinski correlation, the friction factor is assumed to be the Blasius smooth wall, fully-developed, turbulent internal channel flow correlation [14] as described in Equation 1.7.

$$Nu = 0.023 \cdot Re^{0.8} Pr^{0.4} \tag{1.5}$$

$$Nu = \frac{\left(\frac{f}{8}\right)(Re - 1000)\cdot Pr}{1 + 12.7\left(\frac{f}{8}\right)^{0.5}\left(Pr^{2/3} - 1\right)} \tag{1.6}$$

$$f = 0.316 \cdot Re^{-0.25} \tag{1.7}$$

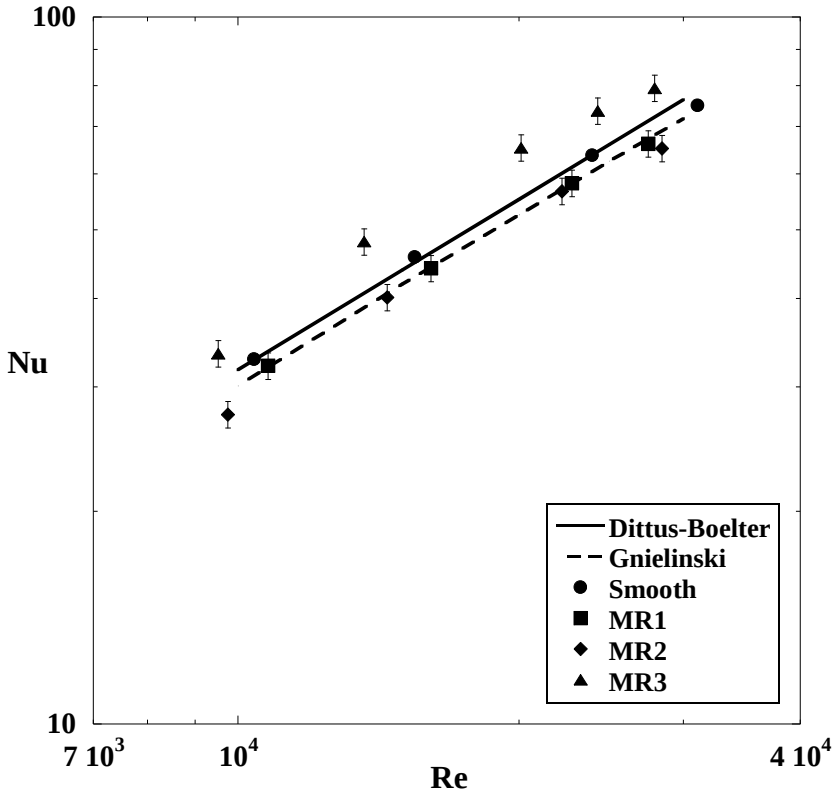

Figure 1.16. Coupon Nusselt number as a function of Reynolds number.

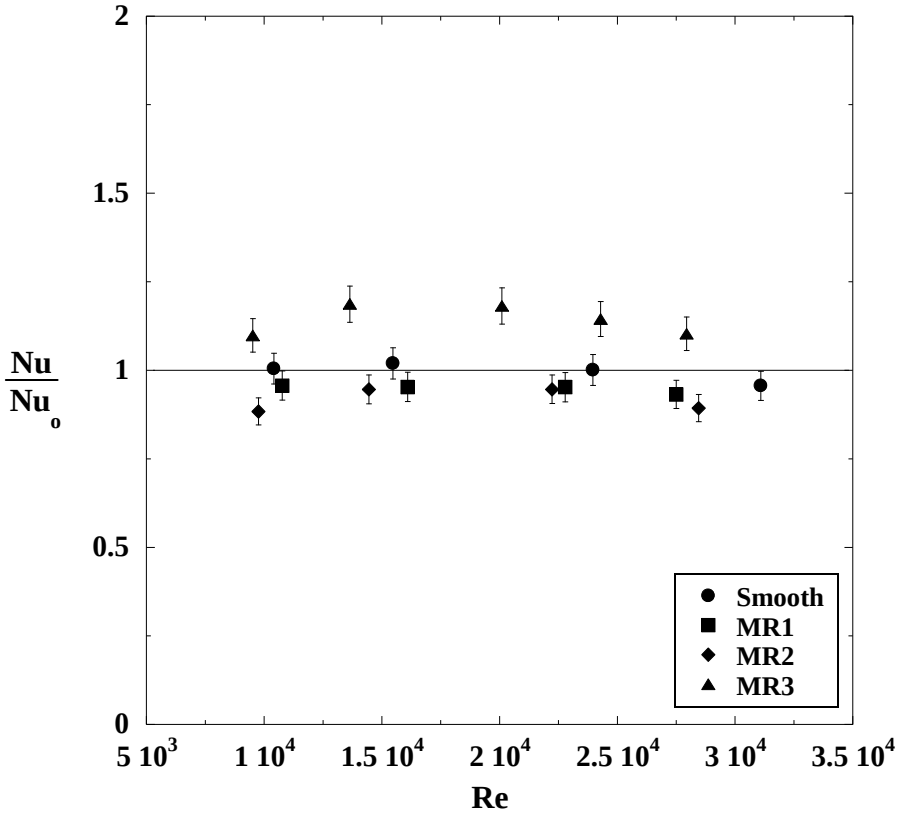

Figure 1.17. Coupon Nusselt number augmentation as a function of Reynolds number.

Figure 1.17 shows the heat transfer augmentation for the four coupons with the Dittus-Boelter correlation used as the assumed smooth wall heat transfer Nusselt number. Within uncertainty, the smooth wall coupon agreed with the smooth wall Dittus-Boelter correlation, with a percent difference of only ±4% through the range of Re numbers tested. Coupons MR1 and MR2 showed no surface roughness effect on heat transfer indicating that average roughness levels of R_a of 2.6 μm and 4.4 μm had no effect. These two roughness levels translate to 1.0% and 1.7% of the channel height, respectively. Coupon MR3, with R_a = 6.1 μm that equated to 2.2% of the channel height, indicated a measurable augmentation on the heat transfer coefficient of the micro channel. This roughness augmented the heat transfer coefficient by 1.1 - 1.2 for Re = $1x10^4$ - $3x10^4$.

Friction Factor Test Results

Experimental results for friction factor are shown below in Figure 1.18 and 1.19. In Figure 1.18, the data is plotted with the Blasius smooth wall correlation as described in Equation 1.7. The smooth wall coupon matched the Blasius correlation well, with a maximum percent difference of 12.3%. As seen in Figure 1.19, the three roughened coupons showed a higher friction factor augmented by 1.8 - 2.6 over the Blasius smooth wall correlation. Coupon MR1 had a friction factor augmentation of 1.8 - 2.0 and Coupon MR2 an augmentation of 2.1 - 2.3, while having no convective heat transfer increase. Coupon MR3 had a slightly higher friction factor augmentation of 2.1 - 2.6, but with a discernable convective heat transfer augmentation as indicated in the previous section.

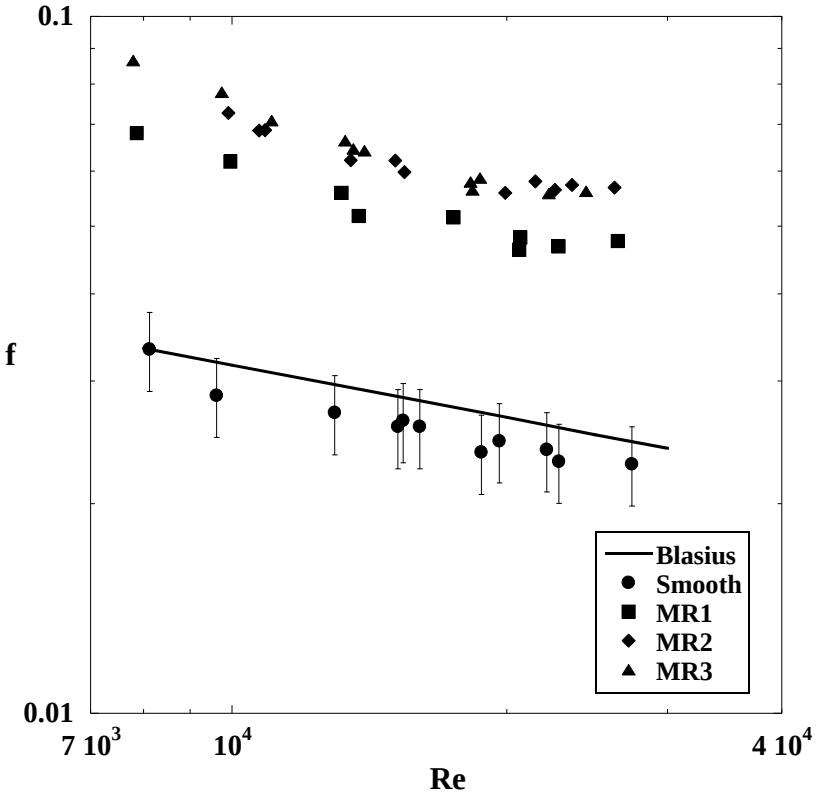

Figure 1.18. Coupon friction factor as a function of Reynolds number.

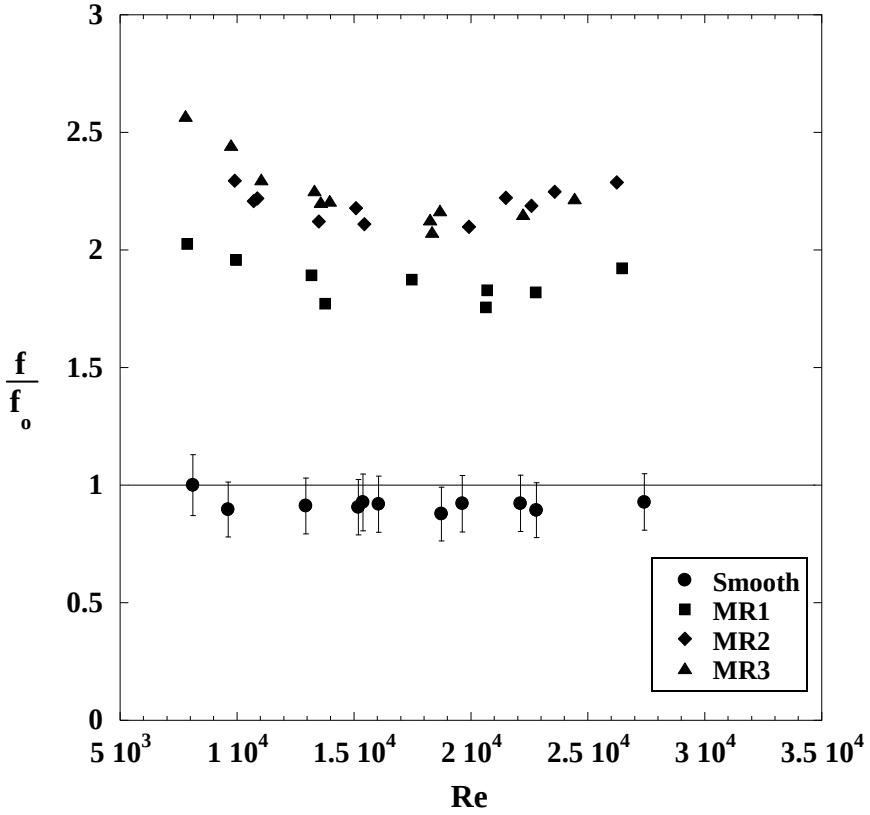

Figure 1.19. Coupon friction factor augmentation as a function of Reynolds number.

The augmentations arising from the heat transfer and friction factor results follow the trend of rib turbulated internal channel flows where the pressure drop is generally augmented by a larger amount over a smooth channel than is the heat transfer. These differences in augmentation between pressure drop and heat transfer have been demonstrated by Park et al. [16] and Han et al. [17]. These differences between augmentation of heat transfer and pressure drop are consistent with the literature and occur as the result of the recirculation regions that occur downstream of the protrusions. These recirculation regions contribute to pressure losses, but do not contribute to additional heat transfer augmentation.

Conclusions

Two test chambers have been developed for quantifying heat transfer coefficients and pressure drops in internal cooling micro channels. At the scale of these channels, the heat transfer and pressure drop can be discernibly affected by the inherent surface roughness due to the manufacturing process. Three roughened channels were manufactured at the level of typical casting techniques, along with a smooth channel to compare to known correlations from the literature. Nusselt numbers and friction factors were reported for the four roughness ratios.

The results for the smooth channel matched the known correlations for Nusselt number and friction factor over the range of Reynolds numbers tested. The channels with R_a = 2.6 μm and 4.4 μm showed no heat transfer augmentation, but did show a friction factor augmentation of 1.8 - 2.3 over the smooth walled channel. The channel with the highest R_a = 6.1 μm showed a heat transfer augmentation of 1.1 - 1.2 and a friction factor augmentation of 2.1 - 2.6.

These results indicate that in the range of known casting techniques, the manufacturing surface roughness has an effect on the heat transfer augmentation when the roughness approaches 2.2% of the channel height. Similar to rib turbulated channels, however, the manufacturing roughness had a much larger impact on the increased pressure losses than on the heat transfer augmentation.

Acknowledgements

The authors would like to thank United Technologies - Pratt & Whitney for sponsoring this research work, along with their partners and advisors Atul Kohli and Christopher Lehane.

References

[1] Bunker, R.S., 2008, "The Effects of Manufacturing Tolerances on Gas Turbine Cooling," ASME Paper No. GT2008-50124.

[2] Avallone, E.A., and Baumeister, T., 1996, Marks' Standard Handbook for Mechanical Engineers (10^{th} ed.). New York: McGraw-Hill Professional, pp. 13-72.

[3] Saini, R.P., and Saini, J.S., 1997, "Heat Transfer and Friction Factor Correlations for Artificially Roughened Ducts with Expanded Metal Mesh as Roughness Element," *International Journal of Heat and Mass Transfer*, Vol. 40, pp. 973-986.

[4] Chang, W.C., Liou, T, and Lu, M.H., 2005, "Heat Transfer of Rectangular Narrow Channel with Two Opposite Scale-Roughened Walls," *International Journal of Heat and Mass Transfer*, Vol. 48, pp. 3921-3931.

[5] Caney, N., Marty, P., and Bigot, J., 2006, "Friction Losses and Heat Transfer of Single-Phase Flow in a Mini-Channel," *Applied Thermal Engineering*, Vol. 27, pp. 1715-1721.

[6] Liu, C.W., Gau, C., and Dai, B.T., 2003, "Design and Fabrication Development of a Micro Flow Heated Channel with Measurements of the Inside Micro-Scale Flow and Heat Transfer Process," *Biosensors & Electronics*, Vol. 20, pp. 91-101.

[7] Qi, S.L., Zhang, P., Wang, R.Z., and Xu, L.X., 2006, "Single-Phase Pressure Drop and Heat Transfer Characteristics of Turbulent Liquid Nitrogen Flow in Micro-Tubes," *International Journal of Heat and Mass Transfer*, Vol. 50, pp 1993-2001.

[8] Lorenzini, M., Morini, G.L., and Salvigni, S., 2010, "Laminar, Transitional and Turbulent Friction Factors for Gas Flows in Smooth and Rough Microtubes," *International Journal of Thermal Sciences*, Vol. 29, pp. 248-255.

[9] Marques, C., and Kelly, K.W., 2004, "Fabrication and Performance of a Pin Fin Micro Heat Exchanger," *Journal of Heat Transfer*, Vol. 126, pp. 434-444.

[10] Bunker, R.S., Bailey, J.C., Lee, C., and Stevens, C.W., 2004, "In-Wall Network (Mesh) Cooling Augmentation of Gas Turbine Airfoils," ASME Paper No. GT2004-54260.

[11] Bunker, R.S., 2009, "A Study of Mesh-Fed Slot Film Cooling," ASME Paper No. GT2009-59338.

[12] Van Rij, J.A., Belnap, B.J., and Ligrani, P.M., 2002, "Analysis and Experiments on Three-Dimensional, Irregular Surface Roughness," *Journal of Fluids Engineering*, Vol. 124, pp. 671-677.

[13] Kline, S.J., and McClintock, F.A., 1953, "Describing Uncertainties in Single-Sample Experiments," *Mechanical Engineering*, Vol. 75, pp. 3-8.

[14] White, F.M., 1994, Fluid Mechanics (3rd ed.). New York: McGraw-Hill College, pp. 313-340.

[15] Incropera, F.P., and DeWitt, D.P., 2002, Fundamentals of Heat and Mass Transfer (5th ed.). New York: John Wiley & Sons, pp. 466-495.

[16] Park, J.S., Han, J.C., Huang, Y., and Ou, S., 1992, "Heat Transfer Performance Comparisons of Five Different Rectangular Channels with Parallel Angled Ribs," *International Journal of Heat and Mass Transfer*, Vol. 35, pp. 2891-2903.

[17] Han, J.C., and Zhang, Y.M., 1992, "High Performance Heat Transfer Ducts with Parallel Broken and V-Shaped Broken Ribs," *International Journal of Heat and Mass Transfer*, Vol. 35, pp. 513-523.

Paper 2: Comparison of Micro Channels Containing Pin Fin Arrays with Available Correlations of Heat Transfer and Pressure Drop

Will be submitted to a future IGTI Turbo EXPO
Co-Authors: M.D. Barringer and K.A. Thole

Abstract

As micro channels continue to be incorporated as an important internal cooling method for gas turbine airfoils, there is concern as to how the heat transfer and pressure drop can be accurately predicted for these small channels using known correlations previously derived from large scale experiments. For the micro channels, manufacturing effects such as surface roughness and tolerances are important considerations on the overall channel heat transfer and pressure drop performance. In addition, at these small scales, the effect of sand ingestion is of importance as sand can adhere to channel surfaces and adversely affect cooling performance. This paper describes an experimental program that measured the heat transfer and pressure drop of micro channels with pin fin arrays before and after sand ingestion. It was shown that heat transfer and pressure drop in clean pin fin arrays can be accurately predicted using correlations derived from large scale tests over a large Reynolds number range. Incremental increases in sand amounts injected at room temperature caused a flow rate reduction in the micro channel cooling air, while engine temperature sand caused a combined reduction in cooling air flow rate and heat transfer performance.

Nomenclature

a	speed of sound
A	area
A_m	flow area between pins
C_p	specific heat
D	pin diameter
f	friction factor: $f = \frac{\Delta P}{2\rho_i V_m^2 N}$
FP	flow parameter: $FP = \frac{\dot{m}\sqrt{T_i \cdot R}}{P_i \cdot A_m}$
FP_0	clean coupon flow parameter

h	convective heat transfer coefficient
H	channel height
k	thermal conductivity
K	loss coefficient
L	coupon length
m_{sa}	sand mass
$\dot{m}$	mass flow rate
N	number of streamwise pin fin rows
Nu_D	Nusselt number: $Nu_D = \frac{h*D}{k_{air}}$
$Nu_{D,0}$	clean coupon Nusselt number
P	pressure
ΔP	pressure difference
ΔP_t	total pressure difference
r	recovery factor: $r = Pr^{1/3}$ [1]
Pr	Prandtl number
PR	pressure ratio: $PR = P_i/P_o$
Q_{net}	net convective heat transfer
Q_H	power from heaters
Q_L	energy loss
R	gas constant
Re_D	Reynolds number: $Re_D = \frac{\rho \cdot V_m \cdot D}{\mu}$
RFP	percent reduction in FP: $RFP = \left.\frac{FP - FP_0}{FP_0}\right\|_{PR}$
S	spanwise pin spacing
SR	Sand ratio: $SR = \frac{m_{sa}}{\dot{m}_{air}}$
T	temperature
ΔT_{LM}	log-mean temperature difference: $\Delta T_{LM} = \frac{(T_s - T_o) - (T_s - T_i)}{\ln\left(\frac{T_s - T_o}{T_s - T_i}\right)}$
V	velocity
V_m	velocity between spanwise pins
W	coupon width
X	streamwise pin spacing
y	vertical distance from channel center

Greek

ρ	density
μ	dynamic viscosity

Subscript

c	coupon
cu	copper
i	inlet
o	outlet
sa	sand
s	surface

Introduction

Since raising air temperatures at the turbine inlet has a direct effect on increasing turbine efficiency, inlet temperatures have increased to the point where they are higher than the airfoil material melting temperatures. To prevent melting during operation, complex internal and external cooling schemes are employed. External cooling methods use film cooling along the airfoil surfaces to provide a boundary layer of cooler air between the hot combustion gases and the blade surface. Bled from the compressor, the supply air for the film cooling is originally routed through internal cooling passages before exhausting through cooling holes placed in the blade surfaces. To increase the cooling performance of the channels, various types of features such as pins, ribs, and dimples are often placed on the channel walls. Along with increasing the cooling surface area of the channel, these features serve to augment the heat transfer coefficient by promoting turbulence and increasing surface area.

A recent trend in internal cooling has been to place micro channels with pin fin arrays within the airfoil walls between the hot external blade surface and internal cooling passage surface. In the past, much of the published laboratory experiments have been performed at large scale where manufacturing is straightforward and where individual cooling effects can be accurately replicated at large scales. To make these micro channels, a new manufacturing technique was developed by the project sponsor. Since there were some unknowns about this technique, particularly in terms of manufacturing tolerances and inherent surface roughness, there has been concern as to whether correlations derived from experiments that used large scale models with matched Reynolds numbers, can be used to accurately predict the heat transfer and pressure drop of micro channels.

Often operating in sandy and dust laden environments, gas turbines can ingest significant amounts of sand and ash that can make its way into almost every component of the engine [2, 3]. Given the small scales of micro channels, there is concern as to how these channels perform after ingesting sand over the course of time. As the sand makes its way through the engine hardware and heats to engine temperatures, the sticky sand collects on airfoil surfaces and solidifies on the cool airfoil surfaces. Sand deposition adversely raises the overall micro channel pressure drop and lowers the cooling performance of the channel, thereby defeating the purpose of adding the extra micro channels to the airfoil structure.

This paper summarizes the results of an experimental program to determine the heat transfer coefficient and pressure drop through various micro channels with pin fin arrays. To determine a clean baseline, experiments were performed on the micro channels before sand injection, and then sand was injected to ascertain the effect of ingestion. Two temperature conditions were considered for these tests: ambient and engine temperature. The baseline was also compared with heat transfer and pressure drop experiments previously measured at large scale [4, 5] to determine whether correlations from large scale tests accurately characterize the micro channels.

Relevant Past Studies

The effect of pin fin arrays on internal channel heat transfer and pressure drop performance has been studied extensively at large scales in the gas turbine field. Metzger et al. [6] was one of the first studies of internal channel heat transfer with various staggered pin fin arrays. They studied circular pin fins with a height to diameter ratio (H/D) = 1, a constant spanwise ratio (S/D) = 2.5, two different streamwise ratios (X/D) = 1.5 and 2.5, and ten streamwise rows. The experiments showed that the denser array had higher overall heat transfer augmentation versus the wider arrays. For each of the arrays, the heat transfer coefficient increased until the fourth to fifth row of pin fins and then remained relatively uniform throughout the rest of the array.

Lawson et al. [4] also studied the effect of staggered circular pin fin arrays on large scale internal channel heat transfer. They studied two different streamwise and spanwise ratios (S/D = 2, 4 and X/D = 1.73, 3.46) at a H/D = 1. Endwall, pin, and array-average overall heat transfer coefficients were measured over a Reynolds number range of $5x10^3$ - $3x10^4$. They showed that

streamwise spacing had a greater effect on the array-average Nusselt number augmentation than did the spanwise spacing. The pin to endwall Nusselt number ratio ranged from 1.4 - 1.85, with the lowest ratio occurring at the largest Reynolds number and densest pin fin array and the largest ratio at the lowest Reynolds number and most open array.

Armstrong et al. [7] performed a literature study on the heat transfer and pressure drop effects of staggered circular pin fin arrays. Matching the Metzger et al. [6] and Lawson et al. [4] results, they found that for a number of pin fin array geometries, the overall heat transfer augmentation over a smooth channel decreased as the streamwise spacing increased. As with the heat transfer, they found that the overall pressure drop decreased as the streamwise spacing increased.

Thrift et al. [5] studied the pressure drop effects of two different S/D and X/D pin fin array ratios with an H/D ratio of one: S/D = 2, X/D = 1.73 and S/D = 4, X/D = 3.46. They showed the pressure drop was a function of pin fin spacing where the denser arrays had higher values across a range of Reynolds numbers versus the wider spaced pin fin arrays. In addition to studying the effect of spanwise and streamwise spacings, they also measured the effect of additional rows to the overall pressure drop. For the same array, no difference on the overall array pressure drop was measured for seven or eight rows.

While micro channel heat transfer is beginning to be studied in the gas turbine field, it has been studied extensively in the electronics cooling industry for refrigerant and boiling flows. Qu et al. [8] and Koşar et al. [9] studied the use of micro channels with pin fin arrays in the cooling of electronic components. Qu et al. used saturated water flow boiling to cool a bank of 0.2 mm by 0.2 mm staggered square pin fins, while Koşar et al. studied single phase and boil inception R-123 flow across 0.1 mm staggered circular pin pins. The studies mainly focused on the effects of the transition to boiling and fully boiling flows.

Gas turbine related micro channels with pin fins were originally studied by Marques et al. [10] at true scale. The channels had a height of 0.5 mm and contained a pin fin array with S/D and X/D ratios of 2.5, and H/D ratio of one. At a Reynolds number up to $2x10^4$, the pin fin array augmented the heat transfer by as much as five times that of a channel containing no pin fins and augmented the friction factor by as much as 20 times. Bunker et al. [11] studied round and diamond pin fin arrays in a channel with a width of 33 cm, height of 0.51 cm, and pin fin array ratios of: S/D =1.5, X/D = 1.5, and H/D = 1. Their findings were that the array increased the

heat transfer performance of the channel by slightly more than two times over a smooth channel, but also increased the friction factor by approximately ten.

The effect of sand ingestion in micro channels with pin fin arrays is lacking in the literature, but has been studied on film-cooling holes by Cardwell et al. [12] and on double-wall cooling designs by Land et al. [13]. Cardwell et al. studied the effects of room temperature and heated sand ingestion on the reduction of air flow through various film-cooling hole geometries. A percent reduction in flow parameter (RFP) of 10 - 20% was found over a clean baseline component, with the larger values at the elevated sand temperatures due to the increased sand tackiness and resulting higher tendency to adhere to the film-cooling holes and liners. Land et al. studied the effects of room temperature sand ingestion on various double-wall cooling designs. Testing over a range of pressure ratios, they found that at a pressure ratio below 1.1 the impingement holes acted as a filter and collected the sand particles. However, at higher pressure ratios, the air carried the sand through the system and the amount of blockage decreased. Blockage was also found to be a function of average particle diameter, as when the sand was filtered to contain the largest 40%, the reduction in cooling air flow was increased by approximately three times.

Unique to the literature, this paper provides the results of an experimental program to determine if previous pin fin turbulated heat transfer and pressure drop data developed at large scale can be used in micro channels. In addition, the effects of sand ingestion at room and engine temperatures on the reduction of micro channel heat transfer and pressure drop performance is reported.

Experimental Apparatus

To determine the effect of pin fin arrays and sand ingestion on micro channel performance, two test stands were constructed. The first test stand allowed for two different chambers to be installed to measure ambient temperature heat transfer and pressure drop performance to compare with correlations. This same test stand was also used to conduct experiments with room temperature sand injection. The second test stand, which involved the use of a heating kiln, contained an apparatus to inject sand at engine temperatures.

The first test stand, as seen in Figure 2.1 [14], was designed to minimize measurement uncertainties and allow for an easy method in changing of the two test chambers. Room

temperature compressed air was supplied to the system at 450 to 620 kPa and was controlled using upstream and downstream regulator valves. The downstream valve allowed the upstream pressure to remain constant while the downstream pressure was regulated to operate at different air mass flow rates. Before reaching the test chamber, the air passed through a filter that removed any impurities that entered the air stream from the upstream piping, a pressure gauge and thermocouple that measured the air properties, and a laminar flow element that measured the mass flow rate of the air. The air then passed into the test chamber and through the coupon micro channel.

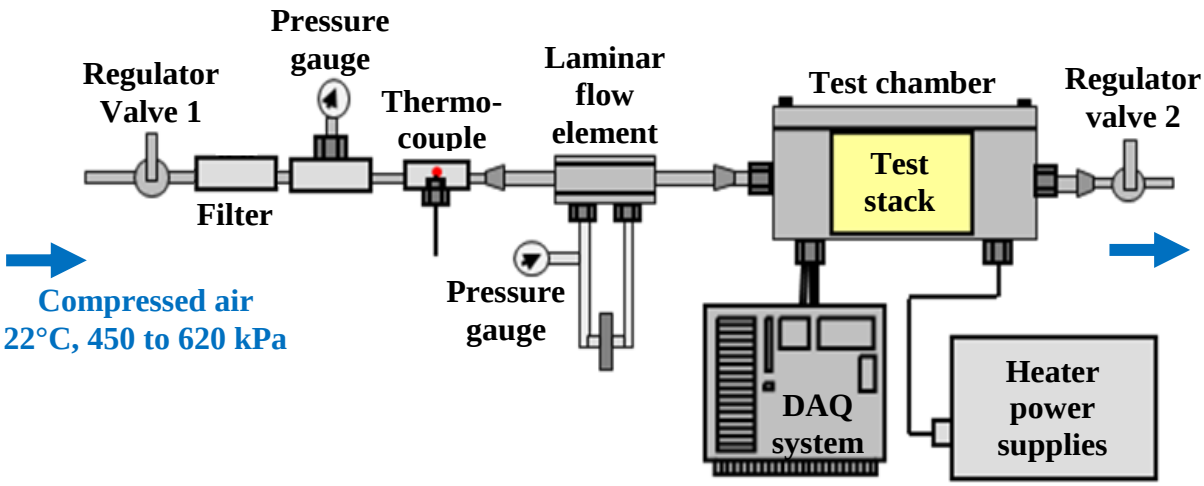

Figure 2.1. Diagram of the overall test apparatus used in this study.

A streamwise sectional view of the heat transfer chamber (test stack as shown in Figure 2.1) is shown in Figure 2.2. The test chamber consisted of a 1.6 cm thick outer enclosure made from polyetheretherketone (PEEK). This hard plastic was chosen for its high tensile strength and low thermal conductivity, as seen in Table 2.1 [14]. Inside this enclosure was an axially centered test stack that contained the coupon, copper heat sinks, electric circuit heaters, and insulating foam. Centrally placing the test stack resulted in identical upstream and downstream chambers, where static pressure and temperature air measurements were made.

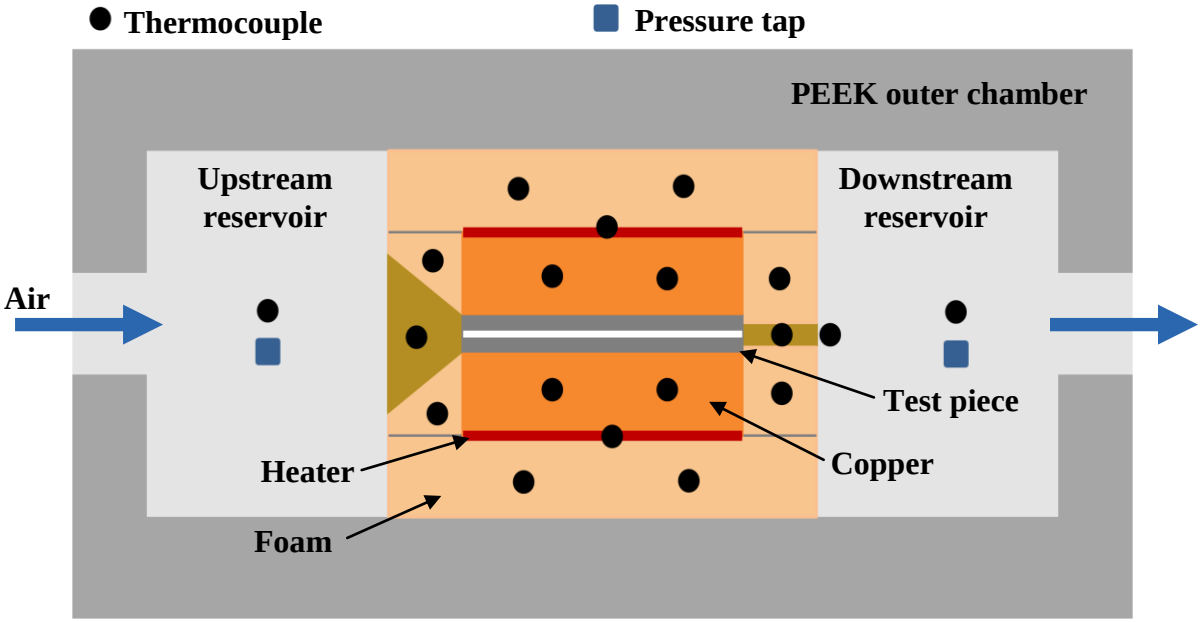

Figure 2.2. Schematic of the heat transfer test stack along instrumentation.

Table 2.1. Heat Transfer Test Stack Thermal Properties

Material	k (W/m K)
Polyetheretherketone (PEEK)	0.25
Copper	400
Insulating Foam	0.054
Thermally Conductive Paste	2.31

The coupon was sandwiched between identical copper heat sinks and electric circuit heaters. The heaters provided a constant heat flux to the copper heat sinks, which then provided a constant temperature boundary condition to the coupon due to the copper's high thermal conductivity as seen in Table 2.1. To minimize the contact resistance at the coupon/heat sink and heater/heat sink interfaces, a thermally conductive paste (properties shown in Table 2.1) was applied in an even serpentine pattern across the surface.

The coupon, heat sinks, and heaters were surrounded by insulating foam with low thermal conductivity, as seen in Table 2.1. This insulation and the PEEK outer enclosure minimized the heat loss through the test stack and chamber to the surrounding atmosphere, which resulted in a heat loss of less than 4% for the overall range of Reynolds numbers tested. Upstream of the coupon, a trapezoidal inlet was integrated into the foam to transition from the

large upstream reservoir to the smaller micro channel. At the exit, a rectangular channel was cut into the foam that allowed the placement of thermocouples at the micro channel and foam exits.

As shown in Figure 2.2, the entire test stack was instrumented with embedded thermocouples to measure the foam, heater, copper heat sink, and air temperatures. Four measurements were made in each of the copper heat sinks to verify an even pitch and transverse temperature distribution, which was important in calculating the micro channel surface temperature using a resistance network described later. The foam temperature measurements were used to calculate the heat loss through the test stack and the outer enclosure to the atmosphere. Three thermocouples upstream of the micro channel in the trapezoidal inlet measured the upstream air properties, while four thermocouples at each of the micro channel and foam exits measured the downstream air properties.

A streamwise sectional view of the pressure drop test chamber is shown in Figure 2.3. The test chamber consisted of an upstream and downstream chamber where static air pressures were measured. To reduce any pressure losses from the large upstream chamber to the micro channel inlet, an inlet nozzle was placed upstream of the channel. The coupon was fixed in place using a compression system that ensured all the flow entered the micro channel and did not pass around it between the nozzle and coupon.

Room temperature sand was injected using a sealed canister and injection pipe. The canister held the sand until a valve was opened and the sand slug fell vertically through the pipe and into the coupon. As with previous sand tests performed by Cardwell et al. [12], the sand was heated in an electric oven at 150 °C for three hours to remove any humidity that tended to cause the sand to combine into large particle groups.

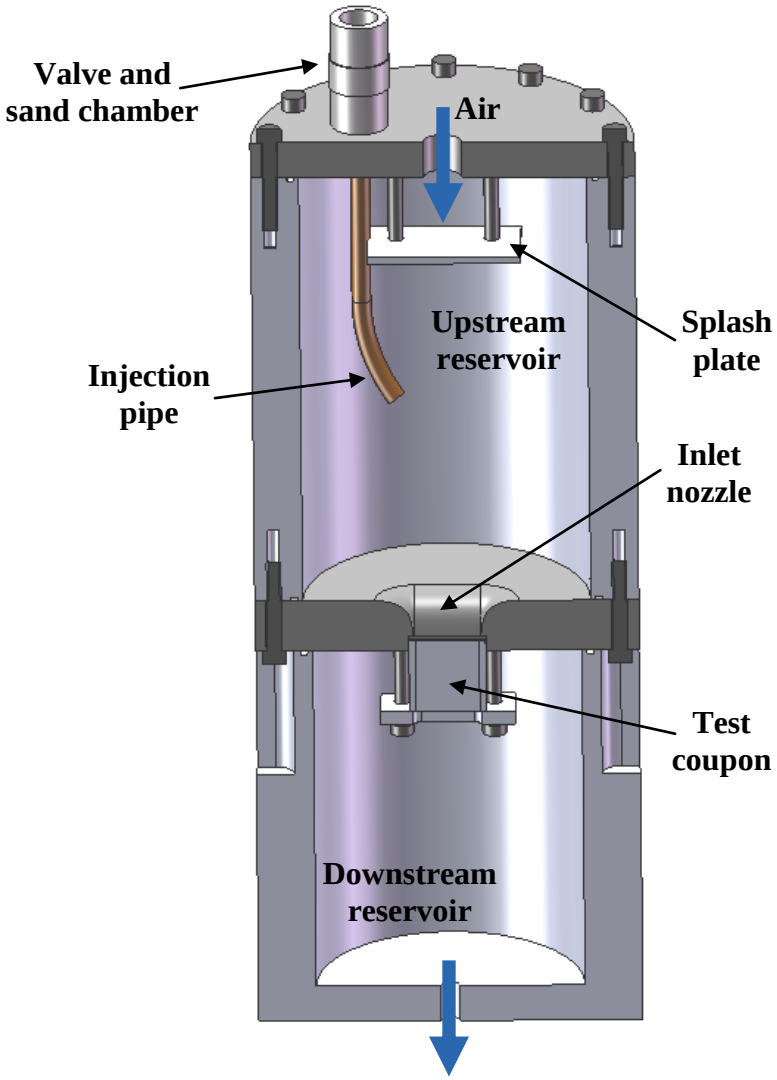

Figure 2.3. Schematic of the pressure drop test chamber.

To determine the effect of engine temperature sand ingestion, a test stand was fabricated that consisted of a simple inlet tube and adapter plate system as seen in Figure 2.4. The coupon was attached to the adapter plate and sealed on all four sides using a high temperature ceramic adhesive. Contrary to the previous room temperature sand injection system, the engine temperature apparatus exhausted to atmospheric pressure and the upstream pressure was varied using a regulator valve. The inlet tube, adapter plate, and coupon were mounted inside an electric kiln and heated to an engine temperature condition of 1060 °C. Air properties were measured using a pressure transducer and thermocouple located upstream of the inlet pipe outside of the kiln.

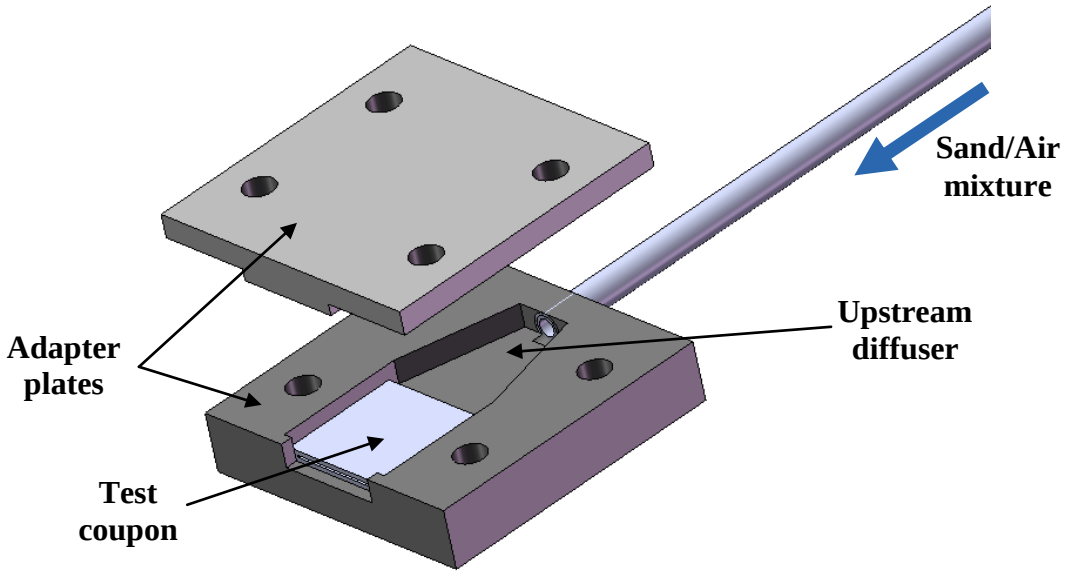

Figure 2.4. Schematic of the engine temperature sand injection apparatus.

The sand was injected using a similar system as the room temperature test stand where a sealed canister held the sand until a valve was opened and the sand slug fell vertically through the inlet tube and into the adapter plate. From the sand residence time in the inlet pipe before reaching the coupon, considerable radiative heating occurred; therefore, this temperature increase was calculated to estimate the sand temperature at the micro channel inlet. From previous tests by Cardwell et al. [12], sand deposition was shown to be a function of sand temperature where higher temperatures resulted in higher deposition percentages. Therefore, for all tests, the sand temperature increase was fixed to where the sand was estimated to be 815 °C when it reached the micro channel inlet. Assuming a mean sand particle diameter of 50 µm and an inlet pipe wall temperature equal to the kiln, the pipe length was calculated to be approximately 18 cm for a Reynolds number of $8x10^3$ as seen in Figure 2.5.

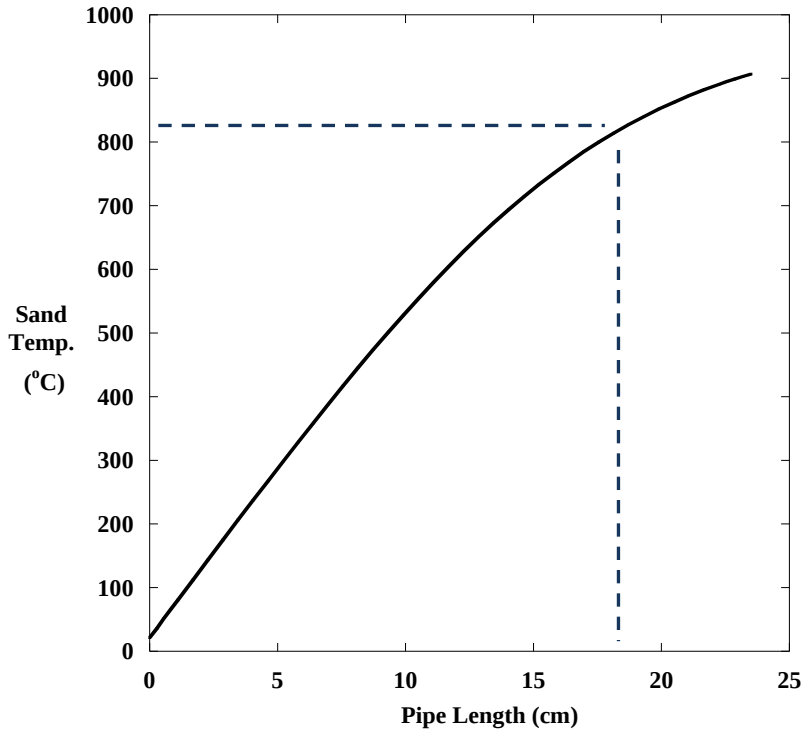

Figure 2.5. Sand temperature increase through inlet pipe.

Description of Pin Fin Coupons

Four coupons were manufactured to determine the pressure drop and heat transfer performance of micro channels with pin fin arrays. The coupons were fabricated using a proprietary technique and material that involved a casting process that quickly and accurately manufactured pin fins with diameters under 1 mm, for a number of array geometries. Each coupon had an overall length (L) and width of 2.54 cm, and a height of 0.25 cm. The internal channel had a width (W) of 2.12 cm and a height (H) of 0.381 mm or 0.508 mm, depending on the coupon. Figure 2.6 shows coupon D, which will be described in detail later, and its internal pin fin array structure and overall geometry.

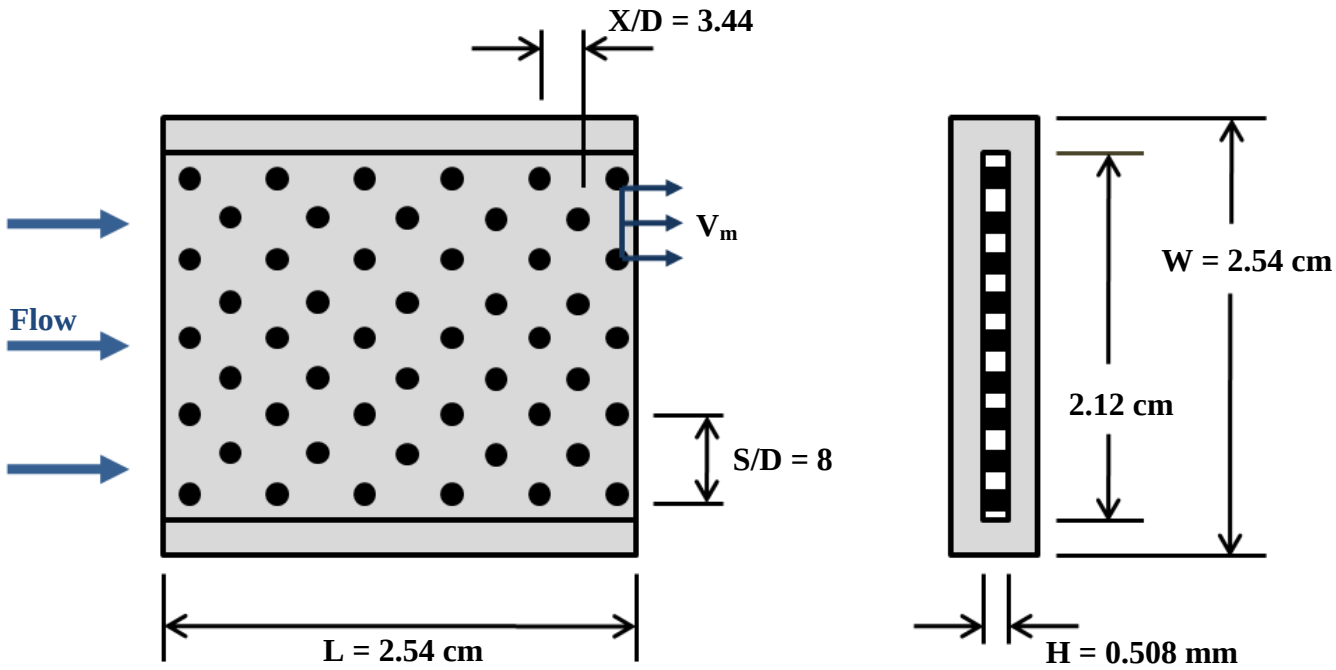

Figure 2.6. Diagram of coupon D and pin fin array ratios.

The coupons were designed and manufactured by the project sponsor to have the same streamwise spacing ratio (X/D), where X was the streamwise distance between pin centers, and the same channel height to pin diameter ratio (H/D). The only difference between the coupons was the spanwise spacing ratio (S/D), where S was the spanwise distance between pin centers. As described in the literature, the S/D ratio was defined using adjacent pins in the same row while the X/D ratio was with adjacent pins in subsequent rows. A schematic of the two spacing ratios are shown in Figure 2.6, along with the characteristic velocity through the pins (V_m) that will be discussed later.

Table 2.2 shows the three ratios (H/D, S/D, and X/D), number of spanwise and streamwise pin fins, and the dimensions that described the four coupons. The H/D and X/D ratios were fixed at approximately 0.8 and 3.5, respectively. The small variation in these two ratios were from coupons A and B having a channel height of 0.381 mm and coupons C and D a height of 0.508 mm. This gave the capability to test two different pin diameters, while still being able to hold the S/D, X/D, and H/D ratios the same. These pin diameters were 0.508 mm for coupons A and B and 0.635 mm for coupons C and D.

Table 2.2. Coupon Geometry

Coupon	Channel height H (mm)	Channel width (mm)	Pin diameter D (mm)	H/D	S/D	X/D	Number of spanwise pin fin rows	Number of streamwise pin fin rows
A	0.381	21.2	0.508	0.75	8	3.50	11	13
B	0.381	21.2	0.508	0.75	4	3.50	21	13
C	0.508	21.2	0.635	0.80	4	3.44	17	11
D	0.508	21.2	0.635	0.80	8	3.44	9	11

Sand Characterization

As characterized by Cardwell et al. [12], Arizona Road Dust was chosen to investigate the effect of sand ingestion on the pin fin arrays. The sand was comprised mainly of different phases of quartz up to 76% along with aluminum oxide, sodium silicate, lime, magnesium oxide, titanium dioxide, and potassium oxide in lesser concentrations. Due to the sand's tendency to group into larger particle masses, Cardwell et al. analyzed the sand particle diameters using a wet and dry laser diffraction analyzer along with a hand sieve analysis. Because the laser diffraction analyzer had a tendency to break the large masses, a smaller particle diameter distribution was found as compared to the hand sieve analysis as seen in Figure 2.7 [12].

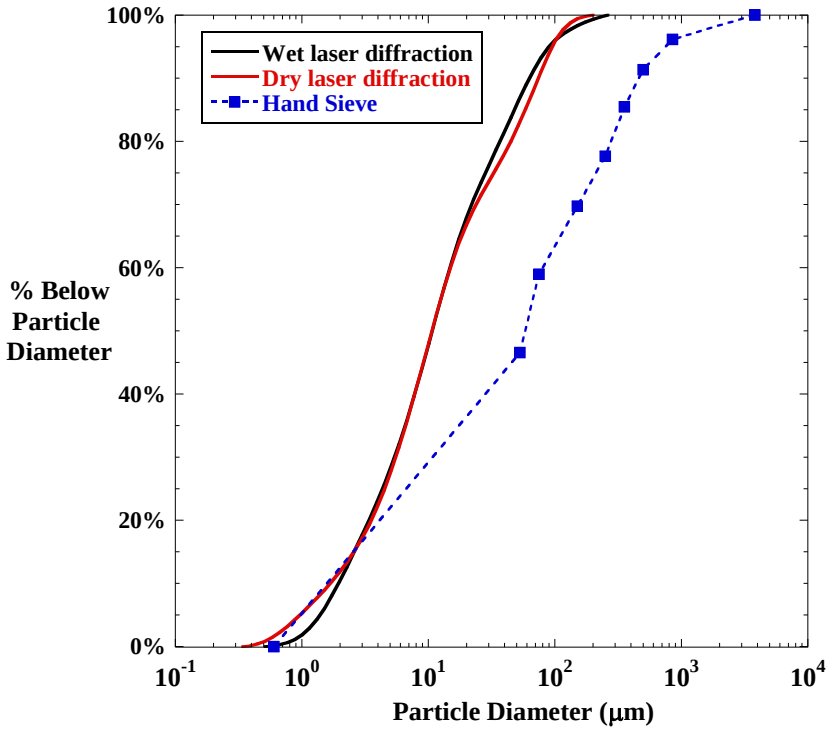

Figure 2.7. Arizona Road Dust particle diameter distribution [12].

Test Method and Data Reduction

As used by Weaver et al. [14], to determine the overall convective heat transfer coefficient (h), the log-mean temperature (ΔT_{LM}) difference, as seen in Equation 2.1, was used. In this equation, Q_{net} is the difference between the power from the heaters and the energy lost to the surroundings ($Q_{net} = Q_H - Q_L$) and A_s is the total channel surface area with pins.

$$Q_{net} = h \cdot A_s \cdot \Delta T_{LM} = \dot{m} \cdot C_p (T_o - T_i) \tag{2.1}$$

The justification in using a temperature difference of this form was based on the micro channel walls having a uniform spanwise and streamwise temperature from channel inlet to exit, as was verified by Weaver et al. [14] through numerical simulations using the finite element computational software ANSYS 11.0. The net difference between the power from the heaters and the energy lost was verified using the first law, as seen in the right side of Equation 2.1. This energy balance compared the amount of measured energy that entered the air using the inlet and outlet temperatures, to the Q_{net} used previously. For coupons B and C the energy balance averaged to within -3% at a $Re_D = 5x10^3$ and 8% at a $Re_D = 2x10^4$, while for A and D the energy balance averaged to within -2% to 12% over the same Reynolds number range. The largest differences occurred at the highest Reynolds numbers where the resulting exit temperature and velocity profiles made it more difficult to measure an average air outlet temperature using the three thermocouples. To account for the higher velocity at the channel exit, the outlet static air temperature was modified using the recovery factor ($r = Pr^{1/3}$) described by Kays and Crawford [1].

Since it was not feasible to measure the micro channel wall temperature at these scales, a thermal resistance network from the copper heat sink midpoint temperature was used. As described by Weaver et al., this resistance network is shown in Equation 2.2 [14].

$$T_s = T_{cu} - \left(0.5 \cdot \Delta y_{cu}\right)\left(\frac{Q_{net}}{k_{cu} \cdot A_{cu}}\right) - \left(\Delta y_c\right)\left(\frac{Q_{net}}{k_c \cdot A_c}\right) \tag{2.2}$$

As seen in Figure 2.8, three resistances occur between the copper midpoint and micro channel wall temperature: copper, thermally conductive paste, and the coupon. Since the paste had a negligible thickness and high conductivity, it was excluded in the resistance network. As

with the micro channel spanwise and streamwise wall temperature variation, Weaver et al. [14] verified this resistance network through ANSYS simulations.

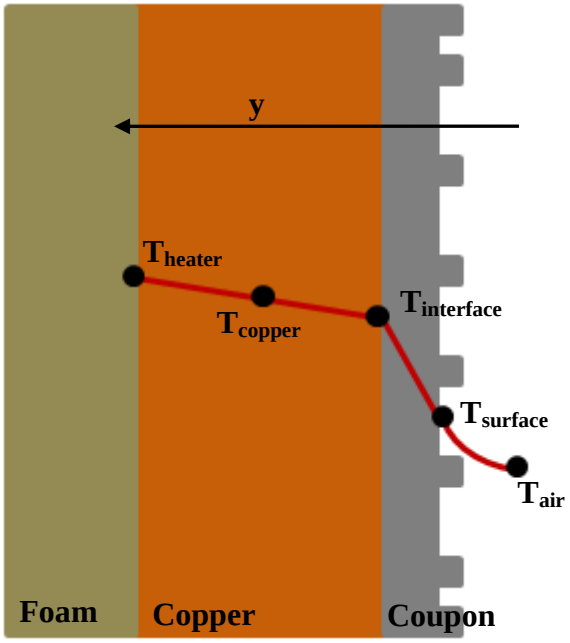

Figure 2.8. Schematic of the heat transfer test stack resistance network.

The overall friction factor for the pin fin array is shown as Equation 2.3. The pressure drop was defined as the total pressure difference between the upstream and downstream chambers, and modified for any micro channel inlet and outlet pressure loss. The sharp micro channel outlet pressure loss coefficient K value was assumed to be 1.0 [15], while the inlet pressure loss was deemed to be negligible due to the upstream nozzle. The customary form of pin fin array friction factor in the literature uses the maximum velocity (V_m) through the coupon that occurs between the pins, as was shown in Figure 2.6. This, along with the number of streamwise pin rows (N), describes the pin fin array geometry in the friction factor equation.

$$f = \frac{\left[\Delta P_t - \frac{1}{2} K \cdot \rho_o \cdot V_o^2\right]}{2\rho_i \cdot V_m^2 \cdot N} \tag{2.3}$$

As described by Walsh et al. [16], the effect of sand ingestion on the pin fin array pressure drop was determined using a pressure ratio of the upstream and downstream micro channel pressures (PR), a flow parameter (FP), and a percent reduction in flow parameter (RFP). These three non-dimensional parameters were used because the sand injection had a

simultaneous effect on the pressure drop and the amount of air that flowed through the pin fin array. The pressure ratio related the inlet and outlet micro channel pressures and was modified for the same pressure loss described in Equation 2.3, while the flow parameter described the amount of air that passed through the channel.

Before the initial sand tests, a clean coupon flow parameter (FP_0) versus PR curve was determined over a range of pressure ratios. This established a clean coupon baseline that the post sand injection coupon was compared to. After each room temperature sand test, the coupon was cleaned and re-measured until the original baseline curve was matched. The RFP described how this sand injection affected the pin fin array at a fixed PR, and related the micro channel FP after sand injection to the clean micro channel FP_0.

To measure the sand effect on the overall pressure drop, the flow was allowed to reach steady state and then the sand was introduced using the valve and injection pipe. After injection, the flow was allowed to reach steady state again and the pressure drop was re-measured. To eliminate any velocity effects from the air entering the upstream chamber on the sand introduction system, a splash plate was installed above the sand injection point.

Uncertainty Analysis

An uncertainty analysis on the heat transfer coefficient was performed by Weaver et al. [14] using the Kline and McClintock [17] partial derivative method. They showed over a range of Reynolds numbers of $1x10^4$ - $3.1x10^4$, the heat transfer coefficient uncertainty varied from 4.1 to 4.3%. The largest uncertainty contributors came from the measured micro channel surface area, copper midpoint average temperature, and air outlet temperature. It should be noted that the energy balances, which is another check, agreed but to within a larger difference than the uncertainty. The reason for this larger discrepancy is that there are also inherent uncertainties in the measured exit temperature.

A similar analysis was performed on the pressure drop test stand to determine the uncertainty in the overall pin fin array friction factor. The overall uncertainty was a function of nine parameters: pressure drop across the micro channel (ΔP), upstream (P_i) and downstream (P_o) pressures, air gas constant (R), air temperature (T), air mass flow rate ($\dot{m}$), channel height (H), channel width (W), and pin fin diameter (D). Over a Reynolds number range of $7.8x10^3$ – $1.9x10^4$, the uncertainty was nominally 10.2%. The largest contributors were the air mass flow

rate, channel height, and pin fin diameter, but a small 0.01 mm uncertainty in the channel height contributed to over 40% of the overall friction factor uncertainty.

The calculation of the uncertainty of the flow parameter was similar to the friction factor uncertainty and consisted of seven parameters: mass flow rate, air temperature and gas constant, upstream pressure, channel height and width, and the pin fin diameter. Over a PR range of 1.1 - 2, an uncertainty of 4.5% was calculated. As with the friction factor, the largest contributors to the uncertainty were the air mass flow rate, channel height, and pin fin diameter.

Friction Factor and Flow Parameter Test Results

Figures 2.9 - 2.13 show the friction factor and flow parameter results for the four clean coupons and for coupon C after room temperature and heated sand injection. In Figure 2.9, the clean micro channel data is plotted compared with that of Thrift et al. [5] who conducted experiments at large scale with a pin fin array geometry of S/D = 4 and X/D = 3.46. Coupons B and C, which had the same pin fin array geometry as Thrift et al., closely matched the friction factor data derived at large scale to within uncertainty, over the range of Re_D numbers tested. While still within uncertainty, the friction factor for coupon B was measured to be approximately 7 - 10% higher than the large scale and coupon C results. This difference comes from the difficulty and highest uncertainty contributor in accurately measuring the micro channel height. While, no large scale data was found in the literature to compare to coupons A and D, it is expected from the literature that the friction factor would be lower for the less dense array.

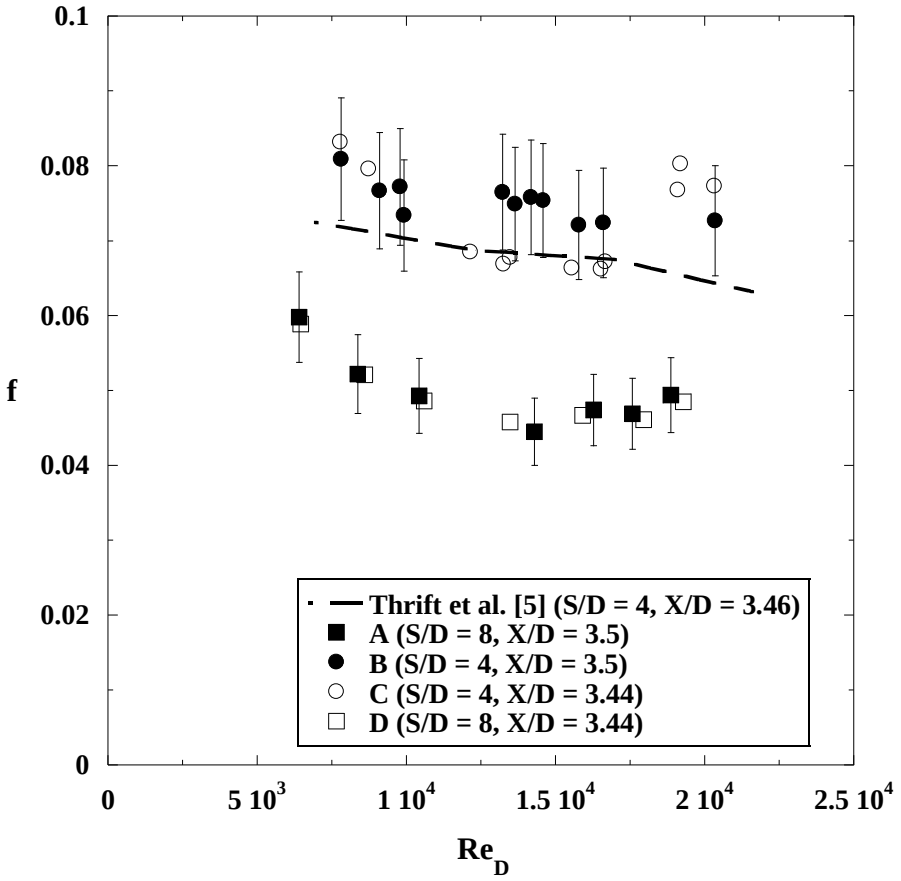

Figure 2.9. Friction factor results for clean coupons compared with a correlation derived from large scale experiments.

Room temperature and heated sand were injected into the micro channel at low and high pressure ratios to measure the effect of sand ingestion on the pin fin array flow parameter. Figures 2.10 - 2.12 show the effect of room temperature sand injection on the flow parameter at various low and high pressure ratios for coupon C. Various sand amounts were injected into the micro channel up to a PR = 1.5. At a SR = 0.4 - 0.44s, the reduction in flow parameter as seen in Figure 2.12, reached a maximum at a PR of approximately 1.07 and then dropped to zero at a PR = 1.43. As with Land et al. [13], at the low pressure ratios, the pin fin array resembled a filter and collected the sand on the upstream surfaces of the pin fins. At the higher pressure ratios, however, the air velocities were high enough to propel the sand directly through the channel and into the channel and pin fin walls which had a tendency to break the sand particles and conglomerations into smaller pieces. At the highest pressure ratio tested, no reduction in flow parameter was found for a SR up to 0.53s (m_{sa} = 3.50g).

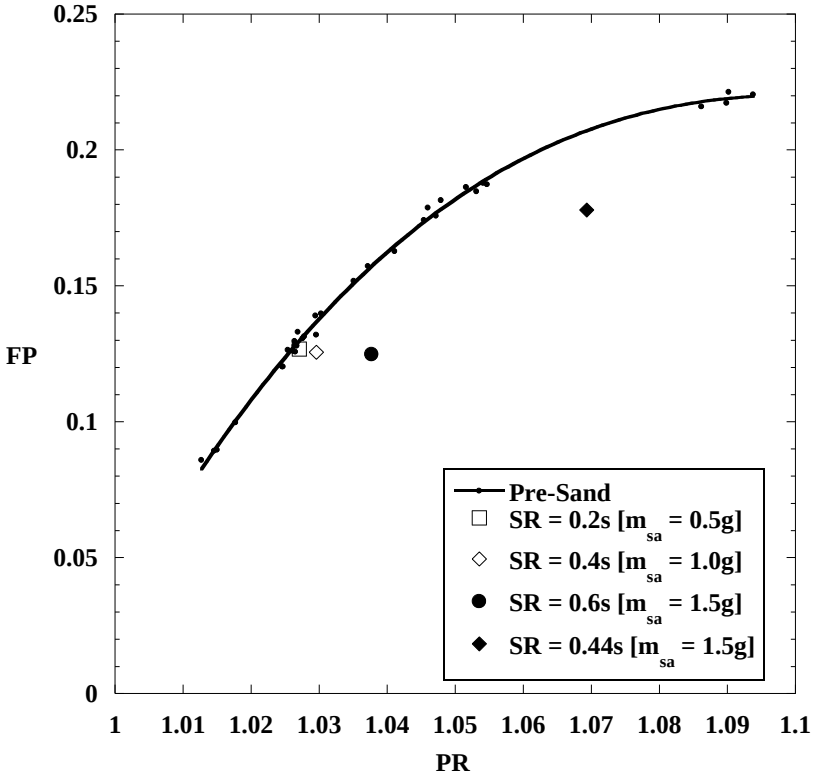

Figure 2.10. Coupon C flow parameter results as a function of pressure ratio for room temperature sand injection (low pressure ratio).

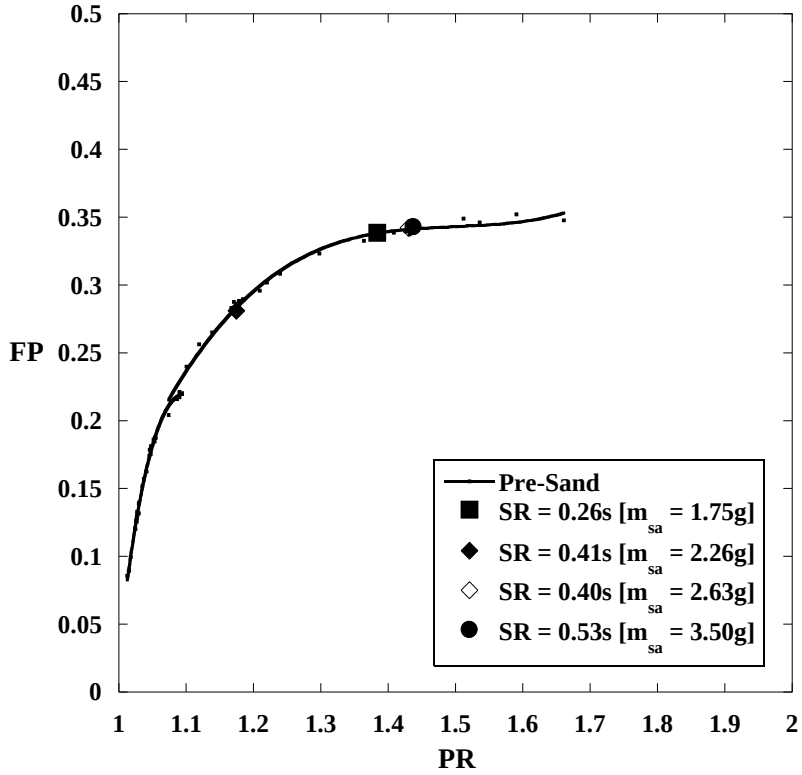

Figure 2.11. Coupon C flow parameter results as a function of pressure ratio for room temperature sand injection (high pressure ratio).

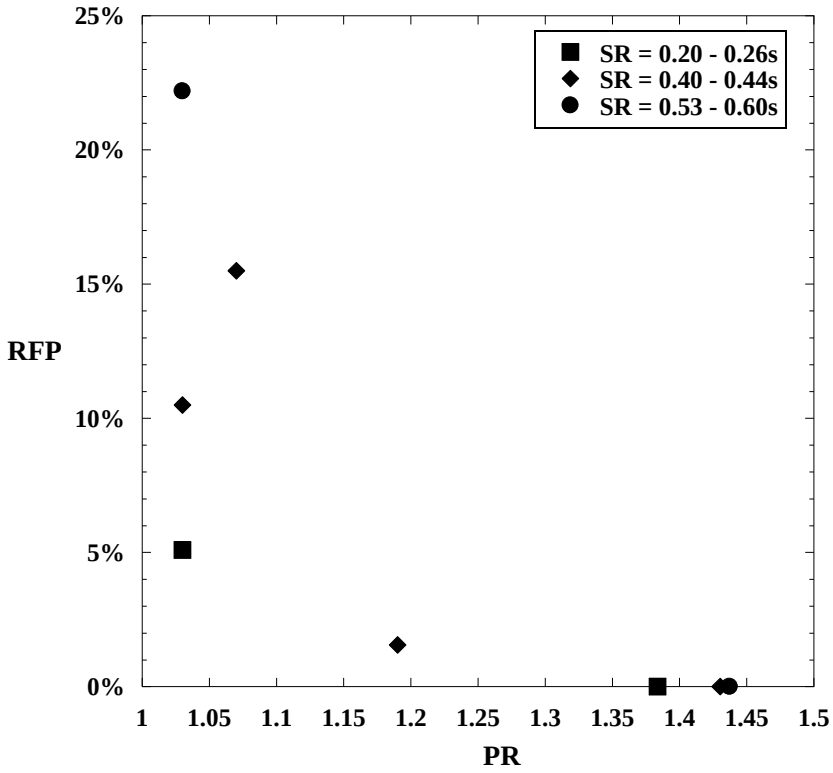

Figure 2.12. Coupon C reduction in flow parameter results as a function of pressure ratio for room temperature sand injection.

The effect of 0.7g of heated sand injected at a PR = 1.03 is shown in Figure 2.13. After injection, the kiln was allowed to cool to room temperature and then the coupon was installed into the pressure drop stand. An average RFP = 15% was measured over a PR range of 1.01 - 1.09. As with the previous experiments by Caldwell et al. [12], a higher RFP was found for the heated sand tests versus the room temperature sand injection tests. For the room temperature sand injection, it took over 1.0g injected at the same pressure ratio to block the channel by the same amount.

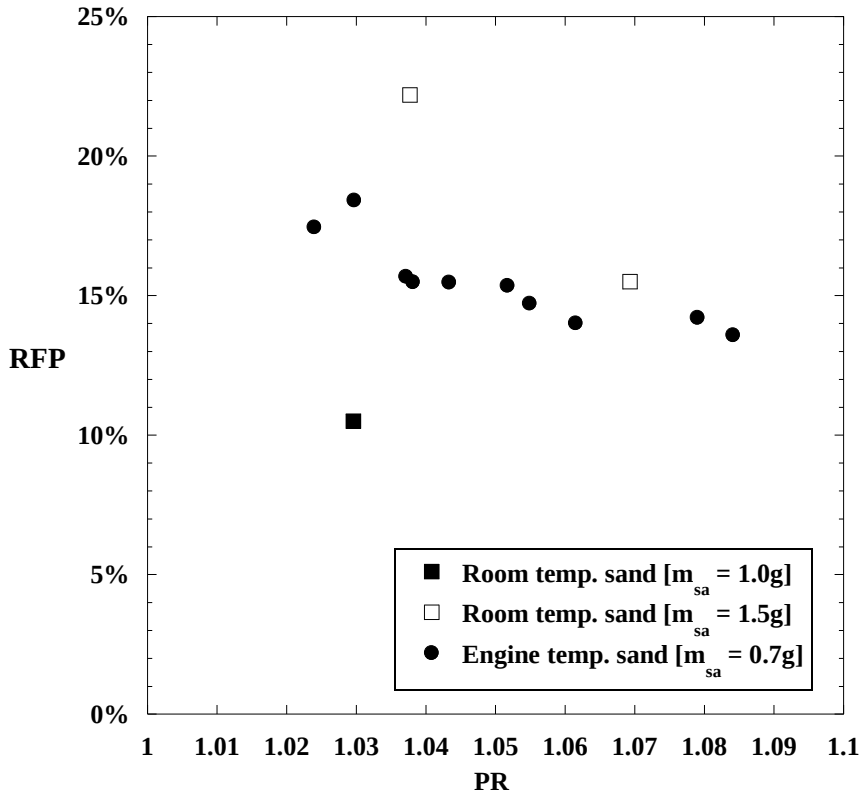

Figure 2.13. Coupon C reduction in flow parameter results as a function of pressure ratio for heated sand injection.

Heat Transfer Test Results

Figures 2.14 - 2.16, show the experimental heat transfer results for the four clean coupons and for coupon C after heated sand injection. Figure 2.14 shows the heat transfer results for the four clean coupons over a Re_D number range of $5x10^3$ - $2.5x10^4$ and is compared with that of Lawson et al. [4] who derived a correlation from large scale testing of a pin fin array with S/D = 4 and X/D = 3.46. As with the friction factor, coupons B and C accurately match the correlation derived from large scale experiments over the range of Reynolds numbers tested. No data at large scale was found in the literature for an array with a S/D = 8 and X/D of approximately 3.5, but as expected, the heat transfer coefficient was found to be lower for the less dense array.

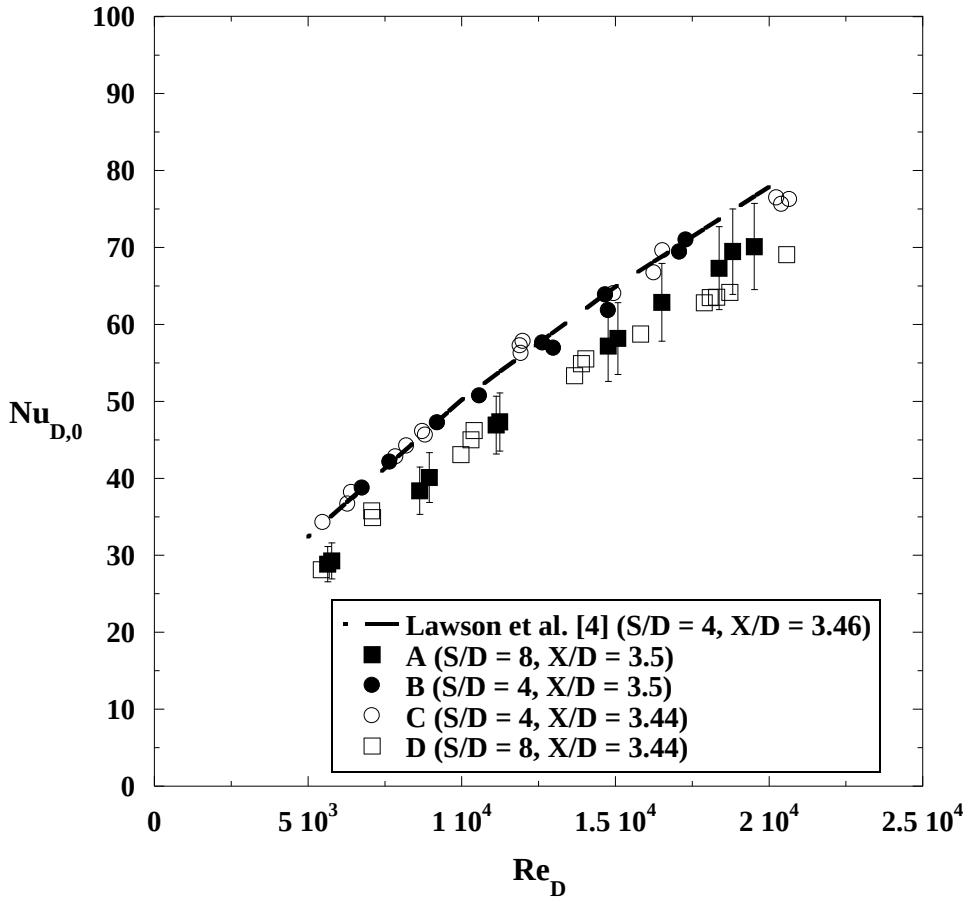

Figure 2.14. Heat transfer results for clean coupons compared with a correlation derived from large scale experiments.

The effect of heated sand on the heat transfer coefficient is shown in Figures 2.15 and 2.16. As with a reduction in the flow parameter, the 0.7g of heated sand injected at a PR = 1.03, caused the heat transfer coefficient to be reduced by approximately 10% at a certain Reynolds number. However, the overall reduction in the heat transfer coefficient is a combination of the reduction in the FP and corresponding decrease in Reynolds number from channel blockage and a reduction in the heat transfer coefficient from the lower conductivity sand adhering to the surface walls. The reduction in the flow parameter is illustrated as the line from 1 to 2 in Figure 2.15 as the drop in Reynolds number, and the reduction in the heat transfer coefficient is shown as the line from 2 to 3. This combined effect is detrimental to engine developers, who designed the cooling channels based off of a known pressure ratio available for internal channel cooling. Channel blockage reduces the flow parameter and hence the actual Reynolds number of the micro channel at the known pressure ratio. This reduction, then combined with the reduction in

the heat transfer coefficient, caused the overall heat transfer reduction to be 24% for the data point at a Reynolds number of approximately $1.5x10^4$. This is over twice as much as the reduction in heat transfer alone.

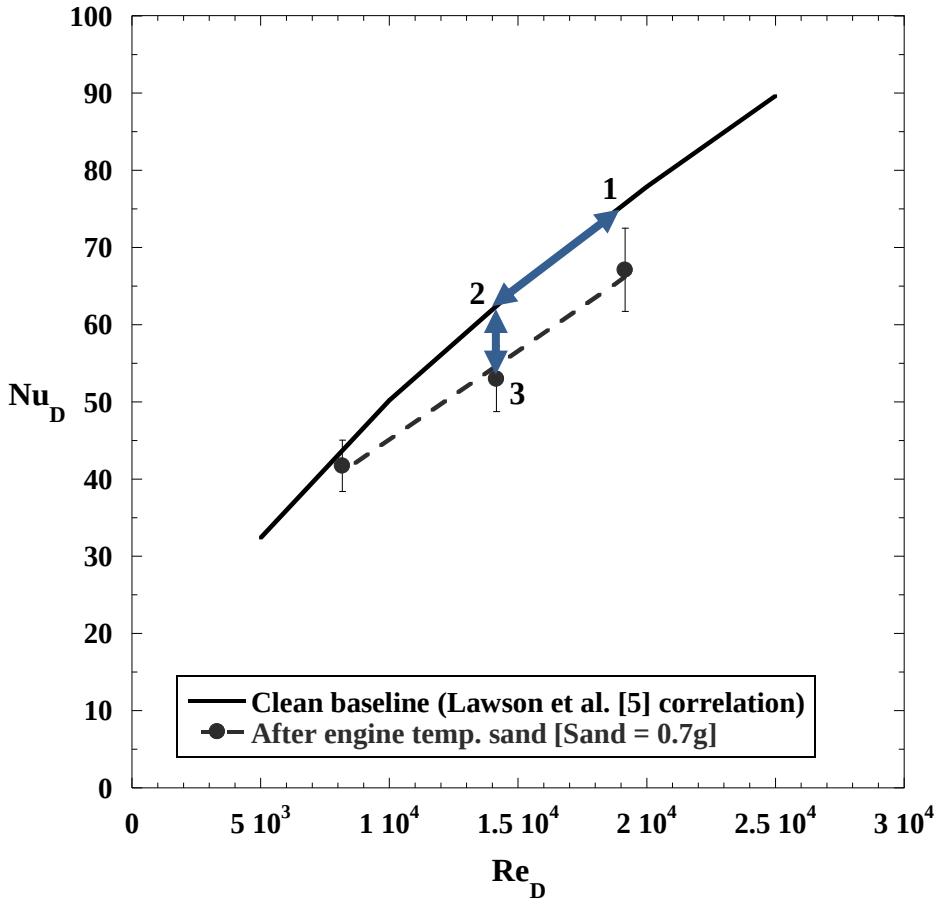

Figure 2.15. Coupon C heat transfer results as a function of Reynolds number for heated sand injection.

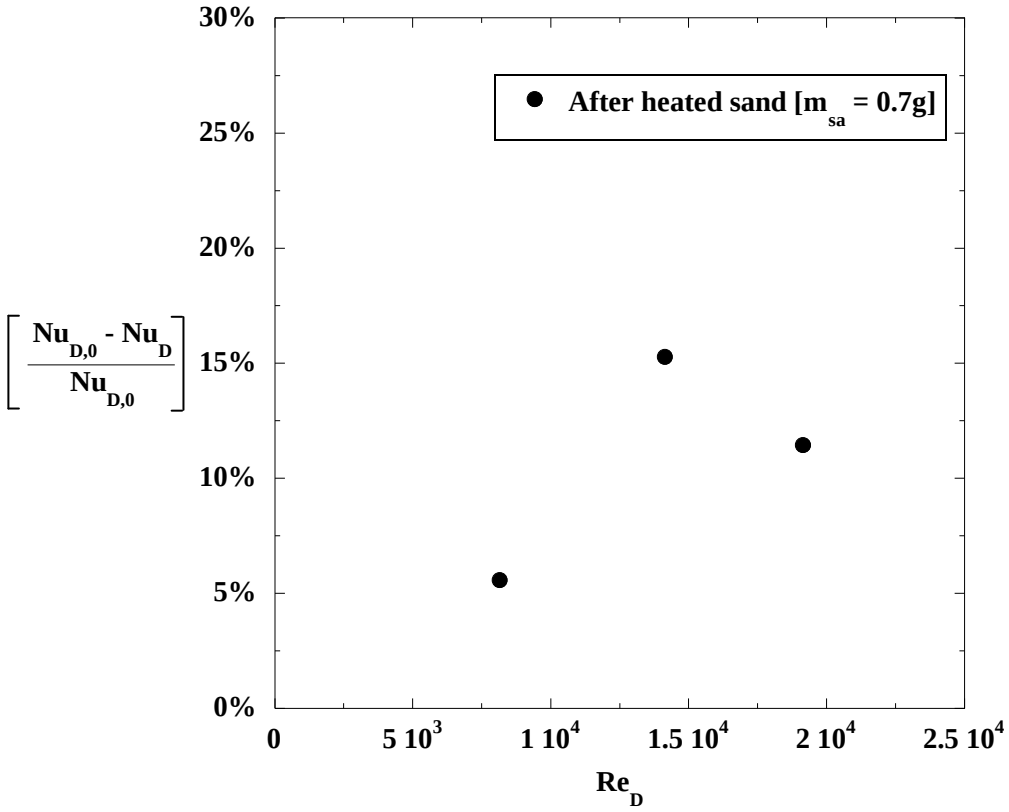

Figure 2.16. Coupon C heat transfer reduction as a function of Reynolds number for heated sand injection.

Conclusions

As micro channels continue to be incorporated into airfoil internal cooling methods, there is concern as to how these small channels compare to previously measured data at large scale due to the manufacturing effects of inherent surface roughness and tolerances. In addition, at these small scales, the effects of engine sand ingestion can adversely affect micro channel heat transfer and pressure drop performance.

An experimental program was developed that measured the heat transfer and pressure drop of micro channels with pin fin arrays before and after sand injection. Comparisons of micro channel data and data from large scale tests indicated that there was good agreement over the entire Reynolds number range tested. To determine the effect of sand ingestion, room temperature and heated sand was injected over a range of pressure ratios. When injected at a low pressure ratio the room temperature sand collected on upstream pin surfaces and reduced the air flow through the channel, while at higher pressure ratios the air velocity was high enough to propel the sand straight through the channel. Heated sand results showed that sand adhered to

the channel surfaces at low pressure ratios and caused a combined reduction in the air flow through the channel, along with a reduction in the heat transfer coefficient.

These results show that previously derived correlations from data measured at large scale can be used to design clean micro channels. Yet care needs to be taken, as these small channels are susceptible to reduced cooling performance over time when sand and dust is ingested by the engine.

Acknowledgements

A special thanks goes to United Technologies - Pratt & Whitney along with Atul Kohli and Christopher Lehane for sponsoring and advising this research work.

References

[1] Kays, W.M., and Crawford, M.E., 1993, Convective Heat and Mass Transfer (3rd Ed.). New York: McGraw-Hill, Inc., pp. 388.

[2] Schneider, O., Benra, F.-K., Dohmen, H.J., and Jarzombek, K., 2005, "A Contribution to the Abrasive Effect of Particles in a Gas Turbine Pre-Swirl Cooling Air System," ASME Paper No. GT2005-68188.

[3] Batcho, P.F., Moller, J.C., Padova, C., and Dunn, M.G., 1987, "Interpretation of Gas Turbine Response Due to Dust Ingestion," ASME Paper No. 1987-GT-112.

[4] Lawson, S.A., 2007, "Heat Transfer From Multiple Row Arrays of Low Aspect Ratio Pin Fins," Thesis, Virginia Polytechnic Institute and State University, Print.

[5] Thrift, A.A., 2007, "Aerodynamic Force and Pressure Loss Measurements on Low Aspect Ratio Pin Fin Arrays," Virginia Polytechnic Institute and State University, Print.

[6] Metzger, D.E., Haley, S.W., 1982, "Heat Transfer Experiments and Flow Visualization for Arrays of Short Pin-Fins," ASME Paper No. 82-GT-138.

[7] Armstrong, J., and Winstanley, D., 1998, "A Review of Staggered Array Pin Fin Heat Transfer for Turbine Cooling Applications," *ASME Journal of Turbomachinery*, 110, pp. 94-103.

[8] Qu, W., and Siu-Ho, A., 2009, "Experimental Study of Saturated Flow Boiling Heat Transfer in an Array of Staggered Micro-Pin-Fins," *International Journal of Heat Transfer*, Vol. 52, pp. 1853-1863.

[9] Koşar, A., and Peles, Y., 2006, "Convective Flow of Refrigerant (R-123) Across A Bank of

Micro Pin Fins," *International Journal of Heat Transfer*, Vol. 49, pp. 3142-3155.

[10] Marques, C., and Kelly, K.W., 2004, "Fabrication and Performance of a Pin Fin Micro Heat Exchanger," *Journal of Heat Transfer*, Vol. 126, pp. 434-444.

[11] Bunker, R.S., Bailey, J.C., Lee, C., and Stevens, C.W., 2004, "In-Wall Network (Mesh) Cooling Augmentation of Gas Turbine Airfoils," ASME Paper No. GT2004- 54260.

[12] Cardwell, N.D., Thole, K.A., and Burd, S.W., 2008, "Investigation of Sand Blocking With Impingement and Film-Cooling Holes," ASME Paper No. GT2008-51351.

[13] Land, C.C., Thole, K.A., Joe, C., 2008, "Considerations of A Double-Wall Cooling Design to Reduce Sand Blockage," ASME Paper No. GT2008-50160.

[14] Weaver, S.A, Barringer, M.D., and Thole, K.A., 2010, "Micro Channels With Manufacturing Roughness Levels," ASME Paper No. GT2010-22976.

[15] White, F.M., 1994, Fluid Mechanics (3rd ed.). New York: McGraw-Hill College, pp. 313-340.

[16] Walsh, W.S., Thole, K.A., and Joe, C., 2006, "Effects of Sand Ingestion on the Blocking of Film-Cooling Holes," ASME Paper No. GT2006-90067.

[17] Kline, S.J., and McClintock, F.A., 1953, "Describing Uncertainties in Single-Sample Experiments," *Mechanical Engineering*, Vol. 75, pp. 3-8.

Conclusions and Summary

As micro channels continue to be incorporated into airfoil internal cooling methods, there is concern as to how well the heat transfer and pressure drop performance of these small channels compare to previously measured data at large scale. For micro channels, inherent manufacturing surface roughness and tolerances could affect the overall channel cooling performance. In addition, at these small scales, the effects of turbine sand ingestion could adversely affect micro channel heat transfer and pressure drop performance.

An experimental program was developed that measured the heat transfer and pressure drop of micro channels with random surface roughness or pin fin arrays with and without sand ingestion. Various coupons were fabricated with levels of surface roughness equal to the resulting roughness from typical casting techniques. The measurements showed that the surface roughness has an effect on the heat transfer augmentation when the roughness approaches 2.2% of the channel height, yet augments the pressure drop at even smaller levels.

In addition, to determine whether correlations developed at large scale can be used to design micro channels with pin fin arrays, various micro channels were fabricated and tested over a range of Reynolds numbers to determine a clean baseline. Furthermore, sand was injected over a range of sand ratios at room and engine temperatures to determine the effect of sand ingestion on micro channel performance. The clean pin fin array heat transfer and friction factor matched the correlations developed at large scale over the range of Reynolds numbers tested. Room temperature sand ingestion at low pressure ratios adversely lowered air flow through the channel, but at higher pressure ratios the effects of sand ingestion were diminished as the higher velocity air forced the sand completely through the channel. Heated sand ingestion was found to have a cumulative effect of lowering air flow at a fixed pressure ratio verse a clean channel, along with lowering the channel heat transfer due to the lower conductivity sand adhering to the channel surfaces.

These results show that previously derived correlations from data measured at large scale can be used to design clean micro channels with pin fin features. Yet care needs to be taken, as these small channels are susceptible to reduced cooling performance over time when sand and dust is ingested by the engine.

Appendix A: Flow Rate and Pressure Drop Calculation

Nomenclature

$A_{0,1,2}$	LFE calibration constants
LFE	laminar flow element
ΔP	pressure difference
Q	volumetric flow rate

Greek

ρ	density
μ	dynamic viscosity

The volumetric flowrate was measured using a 0 - 3.1 CFM (0 – 0.088 m^3/s) Meriam Laminar Flow Element (50MJ10-9). For the specified flowrate range, the corresponding pressure drop of 0 - 8 in. of H_2O (0 – 2 kPa) was measured by a DP103-08 Validyne differential pressure transducer with a 0 - 8.9 in. of H_2O (0 – 2.2 kPa) internal diaphragm. The following figure, Figure A.1, shows a sample performance curve for standard and operating pressures.

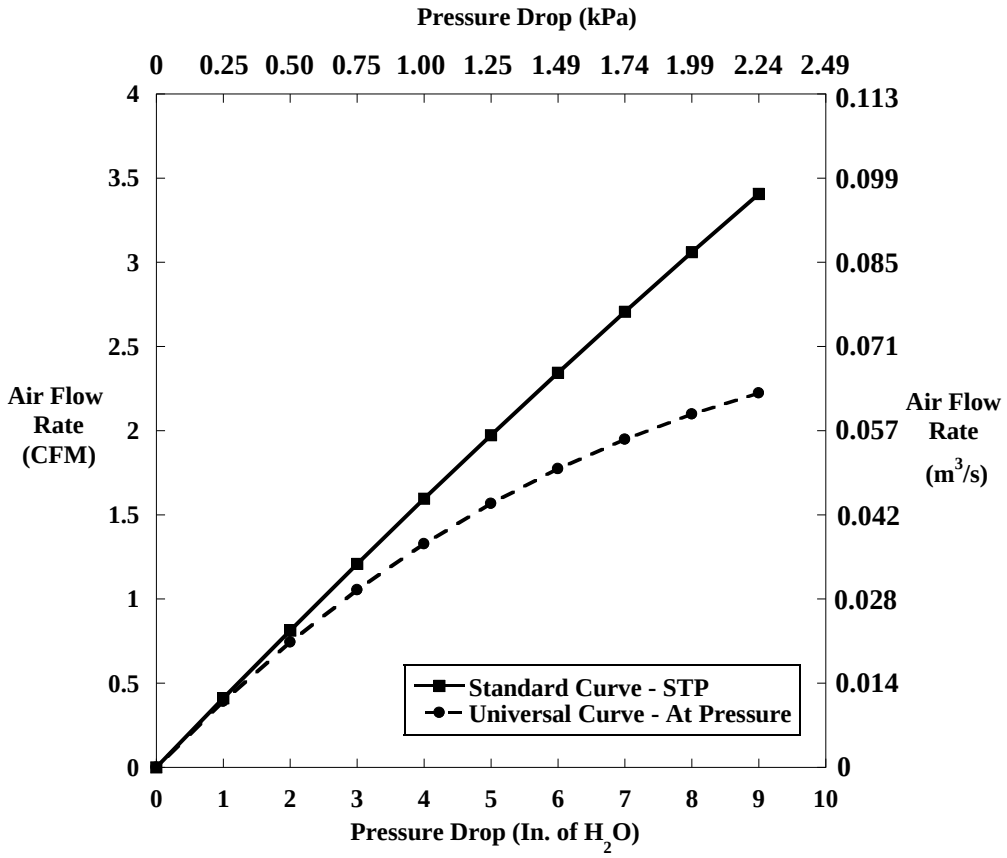

Figure A.1. Sample performance curve for the laminar flow element at standard and operating pressures.

Since the heat transfer and pressure drop stands operated at elevated pressures of 450 - 620 kPa, the performance curve had to be adapted for the difference in pressure from atmospheric. Using three calibration constants (A_0, A_1, and A_2), the inlet air density, and viscosity, the volumetric air flow rate was calculated using Equation A.1 [1]. For the selected LFE, the three constants are shown in Table A.1.

$$Q = A_0 + A_1 \left[\frac{\rho * \Delta P}{\mu^2}\right] + A_2 \left[\frac{\rho * \Delta P}{\mu^2}\right]^2 \qquad \text{(A.1)}$$

Table A.1. Laminar Flow Element Calibration Constants

Constant	Value
A_0	75.571
A_1	-3.5179E05
A_2	5.6852E08

To measure the pressure drop across the coupon from the upstream chamber to the downstream chamber, a separate DP15-IL Validyne differential pressure transducer was employed. This transducer was used for its ability to measure a wide range of pressure ratios using different internal diaphragms. For these tests, the 0 - 20 psi (0 – 137.9 kPa) and 0 - 80 psi (0 – 551.6 kPa) diaphragms were used.

References

[1] Meriam Process Technologies, "Laminar Flow Elements Installation & Operation Instructions," File No. 501:440-11.

Appendix B: Uncertainty Analysis

Nomenclature

A	area
A_m	minimum area
D	pin fin diameter
D_H	hydraulic diameter: $D_H = \frac{2(W \cdot H)}{(W+H)}$
f	friction factor coefficient
FP	flow parameter
FP_0	baseline flow parameter
h	heat transfer coefficient
H	channel height
k	thermal conductivity
K	loss coefficient
L	channel length
$\dot{m}$	mass flow rate
N_{sp}	number of spanwise pin fin rows
N_{st}	number of streamwise pin fin rows
Nu	Nusselt number
P	pressure
ΔP	pressure difference
ΔP_t	total pressure difference
PR	pressure ratio: $PR = P_i/P_o$
Q_{net}	net convective heat transfer
R	gas constant
Re	duct Reynolds number: $Re = \frac{\rho \cdot V \cdot D_H}{\mu}$
Re_D	pin fin Reynolds number: $Re_D = \frac{\rho \cdot V_m \cdot D}{\mu}$
T	inlet temperature
ΔT_{LM}	log-mean temperature difference
u	uncertainty
V	velocity
W	channel width
y	vertical distance from channel center

Greek

ρ	density

μ	dynamic viscosity

Subscript

c	coupon
ch	micro channel
cu	copper
i	inlet
o	outlet
s	surface

An uncertainty analysis was performed on the measured heat transfer coefficient (h), friction factor coefficient (f), and flow parameter (FP) using the method described by Kline and McClintock [1]. The overall heat transfer coefficient and flow parameter equations, as stated previously, are shown in Equation B.1 and B.2 respectively. Due to the slightly different friction factor formulas for the manufacturing roughness coupons (Equation B.3) and the pin fin coupons (Equation B.4), separate uncertainty calculations were performed.

$$h = \frac{Q_{net}}{A_s \cdot \Delta T_{LM}} \tag{B.1}$$

$$FP = \frac{\dot{m}\sqrt{T_i \cdot R}}{P_i \cdot A_m} \tag{B.2}$$

$$f_1 = \frac{\left[\Delta P_t - \frac{1}{2} K \rho_o V_o^2\right] \cdot D_H}{0.5\left(\rho_i \cdot V_i^2\right) \cdot L} \tag{B.3}$$

$$f_2 = \frac{\left[\Delta P_t - \frac{1}{2} K \rho_o V_o^2\right]}{2\rho_i \cdot V_m^2 \cdot N_{st}} \tag{B.4}$$

Heat Transfer Uncertainty

The Kline and McClintock method used the partial derivative technique to relate individual parameter uncertainties to the overall uncertainty. As seen in Equation B.5 for the heat transfer coefficient, this allowed the propagation of all the uncertainties to be summed and incorporated into the overall parameter uncertainty.

$$u_h = \sqrt{\left(\frac{\partial h}{\partial Q_{net}} u_{Q_{net}}\right)^2 + \left(\frac{\partial h}{\partial A_s} u_{A_s}\right)^2 + \left(\frac{\partial h}{\partial \Delta T_{LM}} u_{\Delta T_{LM}}\right)^2} \tag{B.5}$$

Each of the individual parameter uncertainties were performed in the same way. Q_{net} was defined using the total heater power minus the amount lost to the surroundings. The log-mean temperature difference (ΔT_{LM}) was defined as Equation B.6, and related the channel surface, and air inlet and outlet temperatures. The corresponding uncertainty analysis is shown as Equation B.7.

$$\Delta T_{LM} \frac{(T_s - T_o) - (T_s - T_i)}{\ln\left(\frac{T_s - T_o}{T_s - T_i}\right)} \tag{B.6}$$

$$u_{\Delta T_{LM}} = \sqrt{\left(\frac{\partial \Delta T_{LM}}{\partial T_i} u_{T_i}\right)^2 + \left(\frac{\partial \Delta T_{LM}}{\partial T_o} u_{T_o}\right)^2 + \left(\frac{\partial \Delta T_{LM}}{\partial T_s} u_{T_s}\right)^2} \tag{B.7}$$

The micro channel surface temperature was calculated using a resistance network from the measured copper temperatures. This resistance network is shown as Equation B.8, along with the uncertainty analysis as Equation B.9.

$$T_s = T_{cu} - \left(0.5 \cdot \Delta y_{cu}\right)\left(\frac{Q_{net}}{k_{cu} \cdot A_{cu}}\right) - \left(\Delta y_c\right)\left(\frac{Q_{net}}{k_c \cdot A_c}\right) \tag{B.8}$$

$$u_{T_S} = \sqrt{\begin{array}{l}\left(\frac{\partial T_s}{\partial T_{cu}} u_{T_{cu}}\right)^2 + \left(\frac{\partial T_s}{\partial \Delta y_{cu}} u_{\Delta y_{cu}}\right)^2 + \left(\frac{\partial T_s}{\partial Q_{net}} u_{Q_{net}}\right)^2 + \left(\frac{\partial T_s}{\partial k_{cu}} u_{k_{cu}}\right)^2 + \cdots \\ \quad + \left(\frac{\partial T_s}{\partial A_{cu}} u_{A_{cu}}\right)^2 + \left(\frac{\partial T_s}{\partial \Delta y_c} u_{\Delta y_c}\right)^2 + \left(\frac{\partial T_s}{\partial k_c} u_{k_c}\right)^2 + \left(\frac{\partial T_s}{\partial A_c} u_{A_c}\right)^2\end{array}} \tag{B.9}$$

Tables B.1 and B.2 show the uncertainty calculations associated with a low Re and high Re tests. The individual contributions to the overall uncertainty are plotted previously in Figure 1.14.

Table B.1. Heat Transfer Uncertainty (Re = $1x10^4$)

Partial Derivative Term	Value	Uncertainty	Contribution to Overall Uncertainty (%)
Q_H tot. (W)	46.6	0.17	4.8
Q_H indi. (W)	23.3	0.17	0.4
A_s (cm^2)	18.6	0.29	20.5
T_{cu} (K)	344.3	0.28	13.6
Δy_{cu} (cm)	0.318	0.08	1.8
K_{cu} (W/m-K)	400	4	0.07
A_{cu} (cm^2)	6.45	0.014	0.01
Δy_c (cm)	0.1	0.005	5.4
k_c (W/m-K)	8.28	0.08	1.1
A_c (cm^2)	6.45	0.014	0.12
T_i (K)	298	0.11	1.9
T_o (K)	323.9	1.6	50.3
U_h (%)	**4.06**		

Table B.2. Heat Transfer Uncertainty (Re = $3.1x10^4$)

Partial Derivative Term	Value	Uncertainty	Contribution to Overall Uncertainty (%)
Q_H tot. (W)	102.4	0.17	1.9
Q_H indi. (W)	51.2	0.17	0.4
A_s (cm^2)	18.6	0.29	17.9
T_{cu} (K)	338.9	0.28	26.3
Δy_{cu} (cm)	0.318	0.08	3.6
K_{cu} (W/m-K)	400	4	0.14
A_{cu} (cm^2)	6.45	0.014	0.02
Δy_c (cm)	0.1	0.005	11.2
k_c (W/m-K)	8.28	0.08	2.2
A_c (cm^2)	6.45	0.014	0.25
T_i (K)	296.5	0.11	1.9
T_o (K)	315.8	1.6	34.2
U_h (%)	**4.29**		

Friction Factor Uncertainty

The friction factor uncertainty was found in the same way as the heat transfer coefficient. The overall uncertainties for the two friction factors are shown as Equation B.10 and B.11.

$$u_{f_1} = \sqrt{\left(\frac{\partial f_1}{\partial \Delta P_t} u_{\Delta P_t}\right)^2 + \left(\frac{\partial f_1}{\partial \rho_o} u_{\rho_o}\right)^2 + \left(\frac{\partial f_1}{\partial V_o} u_{V_o}\right)^2 + \left(\frac{\partial f_1}{\partial D_H} u_{D_H}\right)^2 + \cdots + \left(\frac{\partial f_1}{\partial \rho_i} u_{\rho_i}\right)^2 + \left(\frac{\partial f_1}{\partial V_i} u_{V_i}\right)^2 + \left(\frac{\partial f_1}{\partial L} u_L\right)^2} \tag{B.10}$$

$$u_{f_2} = \sqrt{\left(\frac{\partial f_2}{\partial \Delta P_t} u_{\Delta P_t}\right)^2 + \left(\frac{\partial f_2}{\partial \rho_o} u_{\rho_o}\right)^2 + \left(\frac{\partial f_2}{\partial V_o} u_{V_o}\right)^2 + \left(\frac{\partial f_2}{\partial \rho_i} u_{\rho_i}\right)^2 + \left(\frac{\partial f_2}{\partial V_m} u_{V_m}\right)^2} \tag{B.10}$$

The inlet and outlet densities were calculated using the upstream and downstream chamber pressures, gas constant, and air temperature, as seen in Equation B.11. The inlet and outlet velocities were calculated using the mass flow rate, channel cross section area, and air density as seen in Equation B.12. For the manufacturing roughness coupons the characteristic flow area was the overall area of the channel (A_{ch} = W*H), while for the pin fin array the characteristic flow area is defined as Equation B.13. The uncertainty calculations for these three parameters are shown in Equations B.14 - B.16.

$$\rho_{i,o} = \frac{P_{i,o}}{R \cdot T_{i,o}} \tag{B.11}$$

$$V_{i,o} = \frac{\dot{m}}{\rho_{i,o} \cdot A_{ch}} \tag{B.12}$$

$$A_{ch} = A_m = \left(W - D \cdot N_{sp}\right) * H \tag{B.13}$$

$$u_{\rho_{i,o}} = \sqrt{\left(\frac{\partial \rho}{\partial P} u_P\right)^2 + \left(\frac{\partial \rho}{\partial R} u_R\right)^2 + \left(\frac{\partial \rho}{\partial T_{i,o}} u_{T_{i,o}}\right)^2} \tag{B.14}$$

$$u_{V_{i,o}} = \sqrt{\left(\frac{\partial V_{i,o}}{\partial \dot{m}} u_{\dot{m}}\right)^2 + \left(\frac{\partial V_{i,o}}{\partial \rho_{i,o}} u_{\rho_{i,o}}\right)^2 + \left(\frac{\partial V_{i,o}}{\partial A_{ch}} u_{A_{ch}}\right)^2} \tag{B.14}$$

$$u_{A_{ch}} = \sqrt{\left(\frac{\partial A_{ch}}{\partial W} u_W\right)^2 + \left(\frac{\partial A_{ch}}{\partial D} u_D\right)^2 + \left(\frac{\partial A_{ch}}{\partial N_{sp}} u_{N_{sp}}\right)^2 + \left(\frac{\partial A_{ch}}{\partial H} u_H\right)^2} \tag{B.15}$$

*For surface manufacturing coupons, N_{sp} = 0.

Tables B.3 and B.4 show the uncertainty calculation associated with the manufacturing roughness coupons. These contributions were previously plotted in Figure 1.15.

Table B.3. Manufacturing Roughness Coupon Friction Factor Uncertainty (Re = $8x10^3$)

Partial Derivative Term	Value	Uncertainty	Contribution to Overall Uncertainty (%)
ΔP (kPa)	3.9	0.02	3.9
P_i (kPa)	620.5	1.55	1.2
P_o (kPa)	616.6	1.54	0.7
R (J/kg-K)	287.1	1.44	3.9
T (K)	293	1	2.7
$\dot{m}$ (kg/s)	1.31E-03	2.62E-05	31.3
H (mm)	0.51	0.013	51.2
W (cm)	1.77	0.005	4.5
L (cm)	5.08	0.005	0.5
U_f (%)	**12.3**		

Table B.4. Manufacturing Roughness Coupon Friction Factor Uncertainty (Re = $3x10^4$)

Partial Derivative Term	Value	Uncertainty	Contribution to Overall Uncertainty (%)
ΔP (kPa)	3.9	0.02	4.0
P_i (kPa)	620.5	1.55	1.1
P_o (kPa)	573.8	1.54	0.9
R (J/kg-K)	287.1	1.44	4.0
T (K)	293	1	2.7
$\dot{m}$ (kg/s)	4.92E-03	2.62E-05	32.0
H (mm)	0.51	0.013	50.3
W (cm)	1.77	0.005	4.6
L (cm)	5.08	0.005	0.4
U_f (%)	**14.3**		

Tables B.5 and B.6 show the uncertainty calculations for the pin fin array coupons. Since only the overall uncertainty was stated previously, Figure B.1 plots the individual contributions at the low and high Reynolds numbers.

Table B.5. Pin Fin Coupon Friction Factor Uncertainty ($Re_D = 7.8x10^3$)

Partial Derivative Term	Value	Uncertainty	Contribution to Overall Uncertainty (%)
ΔP (kPa)	12.2796	0.019554	3.1
P_i (kPa)	721.536	1.5513	1.7
P_o (kPa)	709.257	1.5415	0.2
R (J/kg-K)	287.1	1.44	3.1
T (K)	293	1	2.1
$\dot{m}$ (kg/s)	0.00179	2.62E-05	24.8
H (mm)	0.51	0.013	46.4
W (cm)	1.77	0.005	3.8
D (mm)	0.635	0.025	14.7
U_f (%)	**10.2**		

Table B.6. Pin Fin Coupon Friction Factor Uncertainty ($Re_D = 1.9x10^4$)

Partial Derivative Term	Value	Uncertainty	Contribution to Overall Uncertainty (%)
ΔP (kPa)	12.2	0.02	3.1
P_i (kPa)	723.1	1.55	1.7
P_o (kPa)	710.9	1.54	0.2
R (J/kg-K)	287.1	1.44	3.1
T (K)	293	1	2.1
$\dot{m}$ (kg/s)	1.79E-03	2.62E-05	24.7
H (mm)	0.51	0.013	46.4
W (cm)	1.77	0.005	3.9
D (mm)	0.635	0.025	14.8
U_f (%)	**10.1**		

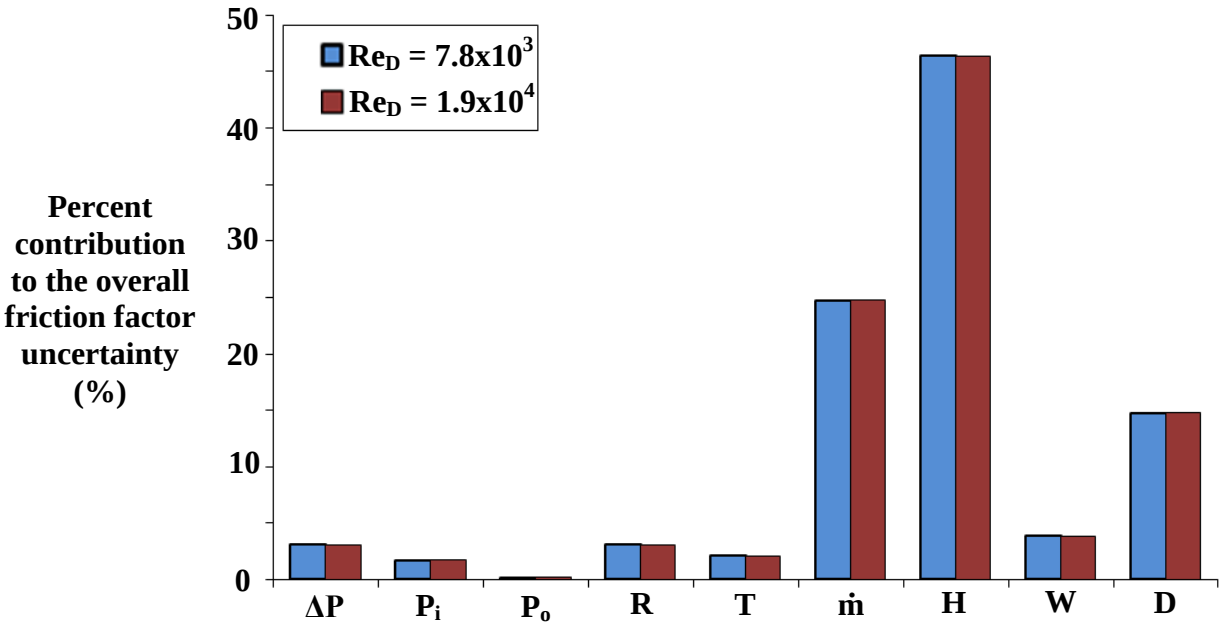

Figure B.1. Parameter percent contribution to the overall pin fin friction factor uncertainty.

Flow Parameter Uncertainty

The uncertainty analysis for the flow parameter is shown in Equation B.15. The characteristic flow rate (A_m) is the same as what was previously described in Equation B.13.

$$u_{FP} = \sqrt{\left(\frac{\partial FP}{\partial \dot{m}} u_{\dot{m}}\right)^2 + \left(\frac{\partial FP}{\partial T_i} u_{T_i}\right)^2 + \left(\frac{\partial FP}{\partial R} u_R\right)^2 + \left(\frac{\partial FP}{\partial P_i} u_{P_i}\right)^2 + \left(\frac{\partial FP}{\partial A_m} u_{A_m}\right)^2} \qquad \text{(B.15)}$$

Table B.7 shows the uncertainty calculations for the flow parameter at a $Re_D = 2.4x10^4$. A separate uncertainty analysis was performed at a $Re_D = 8.9x10^3$, but the individual contributions to the overall uncertainty and the overall uncertainty were identical. Figure B.2 plots the individual contribution for the two Reynolds numbers.

Table B.7. Pin Fin Coupon Flow Parameter Uncertainty ($Re_D = 2.4x10^4$)

Partial Derivative Term	Value	Uncertainty	Contribution to Overall Uncertainty (%)
P_i (kPa)	729.8	1.82	3.1
R (J/kg-K)	287.1	1.44	3.1
T (K)	295	1	2.2
$\dot{m}$ (kg/s)	1.79E-03	4.08E-05	24.7
H (mm)	0.51	0.013	46.2
W (cm)	1.77	0.005	4.0
D (mm)	0.635	0.025	16.8
U_f (%)	**4.49**		

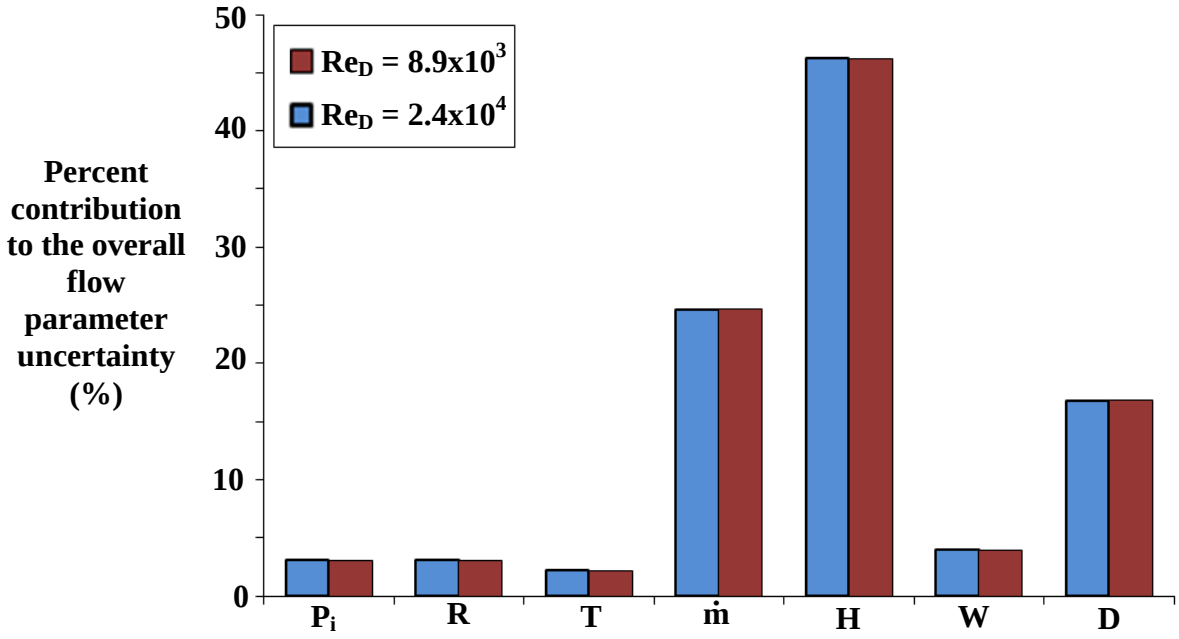

Figure B.2. Parameter percent contribution to the overall pin fin flow parameter uncertainty.

References

[1] Kline, S.J., and McClintock, F.A., 1953, "Describing Uncertainties in Single-Sample Experiments," *Mechanical Engineering*, Vol. 75, pp. 3-8.

Appendix C: Heat Transfer, Friction Factor, and Flow Parameter Results

Nomenclature

A	area
A_m	minimum area
D	pin fin diameter
D_H	hydraulic diameter: $D_H = \frac{2(W \cdot H)}{(W+H)}$
f_1	friction factor: $f_1 = \frac{\Delta P}{0.5\left(\rho_i \cdot V_i^2\right)} \frac{D_H}{L}$
f_2	friction factor: $f_2 = \frac{\Delta P}{2\rho_i V_m^2 N}$
FP	flow parameter: $FP = \frac{\dot{m}\sqrt{T_i \cdot R}}{P_i \cdot A_m}$
FP_0	baseline flow parameter
k	thermal conductivity
L	channel length
Nu	Nusselt number: $Nu = \frac{h \cdot D_H}{k_{air}}$
Nu_D	Nusselt number: $Nu_D = \frac{h \cdot D}{k_{air}}$
P	pressure
ΔP	pressure difference
PR	pressure ratio: $PR = P_i/P_o$
R	gas constant
Re	duct Reynolds number: $Re = \frac{\rho \cdot V \cdot D_H}{\mu}$
Re_D	pin fin Reynolds number: $Re_D = \frac{\rho \cdot V_m \cdot D}{\mu}$
RFP	percent reduction in FP: $RFP = \left.\frac{FP - FP_0}{FP_0}\right\|_{PR}$
V	velocity
V_m	velocity between spanwise pins

Greek

ρ	density
μ	dynamic viscosity

Subscript

i	inlet

o outlet

Heat Transfer Results

The following tables (Tables C.1 – C.5) show the heat transfer results for all the manufacturing roughness and pin fin array tests. Table C.1 shows the heat transfer results for the baseline smooth coupon and the three roughened surface coupons.

Table C.1. Manufacturing Roughness Coupon Heat Transfer Results

Smooth		MR1		MR2		MR3	
Re	**Nu**	**Re**	**Nu**	**Re**	**Nu**	**Re**	**Nu**
15475	45.7	16099	44.1	14447	40.14	13643	48.1
23973	63.7	10771	32.1	22230	56.7	20109	65.3
31090	74.9	22790	58.2	9758	27.4	24286	73.6
10408	32.8	27505	66.2	28459	65.2	9522	33.4
						27941	79.3

Pratt & Whitney provided five tests coupons for each of the pin fin array geometries to also determine if there was any manufacturing variability. Every coupon was not tested. In the flowing tables (Table C.2 – C.5), the coupons are described as A1, A2, etc.

Table C.2. Pin Fin Coupon A Heat Transfer Results

A2		A5	
Re_D	**Nu_D**	**Re_D**	**Nu_D**
5766	29.3	5637	28.9
11118	46.9	11236	47.4
14771	57.2	15084	58.2
18810	69.5	16508	62.9
8632	38.4	18374	67.3
		8944	40.1
		19516	70.2

Table C.3. Pin Fin Coupon B Heat Transfer Results

B1		B2	
Re_D	**Nu_D**	**Re_D**	**Nu_D**
7661	42.1	6764	38.8
10578	50.8	12629	57.6
14772	61.9	9202	47.3
12978	56.9	17288	71.0
17079	69.5	14680	63.9

Table C.4. Pin Fin Coupon C Heat Transfer Results

C1		C3		C4	
Re_D	Nu_D	Re_D	Nu_D	Re_D	Nu_D
6293	36.7	6407	38.2	5478	34.3
8820	45.7	8730	46.1	7852	42.9
11928	56.3	11997	57.9	8198	44.3
16245	66.8	16541	69.6	11904	57.3
20407	75.7	20244	76.5	14944	64.1
				20661	76.3

Table C.5. Pin Fin Coupon D Heat Transfer Results

D1		D2	
Re_D	Nu_D	Re_D	Nu_D
7094	34.9	5428	28.1
10296	45.0	9968	43.1
13897	54.9	13668	53.4
18299	63.6	15823	58.8
7066	35.8	18092	63.5
10404	46.2	18725	64.2
14040	55.6	17897	62.8
20569	69.1		

Table C.6 show the heat transfer results after 0.7g of heated sand was injected into coupon C at a PR = 1.03.

Table C.6. Pin Fin Coupon C Heat Transfer Results After Heated Sand Injection

Re_D	Nu_D
8167	41.8
14149	53
19156	67.1

Friction Factor Results

The friction factor results for all the manufacturing roughness and pin fin array coupons are shown in Tables C.7 – C.11. Table C.7 shows the friction factor results for the baseline smooth coupon and the three roughened surface coupons. Tables C.8 – C.11 show the friction factor results for the four pin fin array geometry coupons before sand was injected.

Table C.7. Manufacturing Roughness Coupon Friction Factor Results

Smooth		MR1		MR2		MR3	
Re	**f_1**	**Re**	**f_1**	**Re**	**f_1**	**Re**	**f_1**
9623	0.0286	7867	0.068	9908	0.0727	13969	0.0642
15396	0.0263	13761	0.0517	15093	0.0621	22231	0.0557
16062	0.0258	20640	0.0463	23586	0.0573	7796	0.0864
19630	0.0246	26475	0.0476	13500	0.0622	18254	0.0579
22122	0.0239	22782	0.0468	21486	0.0580	24433	0.0561
6579	0.0347	20697	0.0482	10713	0.0686	13581	0.0645
8123	0.0333	17481	0.0515	19917	0.0558	18693	0.0586
15194	0.0258	13189	0.0558	15451	0.0598	11047	0.0709
18748	0.0237	9965	0.0619	10864	0.0687	18344	0.0564
22802	0.0230			22592	0.0564	9749	0.0778
27418	0.0228			26237	0.0568	13306	0.0663
12953	0.0270						

Table C.8. Pin Fin Coupon A Friction Factor Results

A4	
Re_D	**f_2**
6408	0.0598
10426	0.0493
14291	0.0445
8366	0.0522
16271	0.0474
17583	0.0469
18873	0.0494

Table C.9. Pin Fin Coupon B Friction Factor Results

B1		B2	
Re_D	**f_2**	**Re_D**	**f_2**
7816	0.0809	9099	0.0767
13226	0.0765	15779	0.0721
16603	0.0724	13647	0.0749
14174	0.0758	9923	0.0734
9786	0.0772	14577	0.0754
20356	0.0727		

Table C.10. Pin Fin Coupon C Friction Factor Results

C3		C5	
Re_D	f_2	Re_D	f_2
8734	0.0796	7783	0.0832
12154	0.0685	13254	0.0669
13482	0.0678	15548	0.0664
16524	0.0662	16664	0.0672
19099	0.0768	19187	0.0803
20326	0.0773		

Table C.11. Pin Fin Coupon D Friction Factor Results

D1	
Re_D	f_2
6453	0.0589
8605	0.0521
10597	0.0486
13471	0.0458
15909	0.0467
17958	0.0461
19287	0.0485

Flow Parameter Results

Before the effect of sand ingestion was studied, a clean baseline curve was measured at low PR (<1.1) and high PR (>1.1) as seen in Table C.12. The low PR and high PR room temperature sand injection tests are shown in Table C.13 and C.14. The data RFP versus PR for the heated sand injection test is shown in Table C.15.

Table C.12. Pin Fin Coupon C Baseline Flow Parameter Results

Low PR (< 1.1)		High PR (> 1.1)	
PR	**FP_0**	**PR**	**FP_0**
1.0351	0.1518	1.0737	0.2043
1.015	0.0897	1.1006	0.2399
1.0472	0.1757	1.4320	0.3373
1.0547	0.1873	1.1192	0.2565
1.0938	0.2204	1.1846	0.2898
1.0146	0.0892	1.6607	0.3477
1.0177	0.0997	1.1387	0.2652
1.0303	0.1398	1.2398	0.3085
1.0411	0.1627	1.3640	0.3328
1.0541	0.1878	1.1710	0.2876
1.0902	0.2213	1.2981	0.3234
1.0862	0.2160	1.4256	0.3398
1.0296	0.1320	1.5361	0.3461
1.0454	0.1742	1.5121	0.3492
1.0295	0.1390	1.5906	0.3522
1.0372	0.1573	1.2198	0.3020
1.0516	0.1863	1.1793	0.2885
1.0899	0.2173	1.2096	0.2959
1.0127	0.0859	1.4082	0.3386
1.0264	0.1279	1.1751	0.2794
1.0262	0.1260	1.1779	0.2881
1.0254	0.1264	1.1673	0.2833
1.0246	0.1203		
1.0267	0.1279		
1.0269	0.1330		
1.0276	0.1306		
1.0247	0.1202		
1.0278	0.1314		
1.0265	0.1257		
1.0264	0.1296		
1.0531	0.1847		
1.0460	0.1788		
1.0479	0.1814		

Table C.13. Pin Fin Coupon C Low Pressure Ratio Room Temperature Sand Results

Low PR (< 1.1)				
Sand [g]	**SR [s]**	**PR**	**FP**	**RFP (%)**
0.50	0.2	1.0278	0.1253	7.52
0.50	0.2	1.0257	0.1268	1.90
0.50	0.2	1.0279	0.1279	5.88
0.50	0.2	1.0261	0.1284	1.57
1.00	0.4	1.0300	0.1273	10.09
1.00	0.4	1.0308	0.1289	10.30
1.00	0.4	1.0279	0.1206	11.24
1.50	0.44	1.0420	0.1284	24.63
1.50	0.44	1.0355	0.1217	21.83
1.50	0.44	1.0356	0.1243	20.24
1.50	0.6	1.0664	0.1742	16.26
1.50	0.6	1.0667	0.1796	13.76
1.50	0.6	1.0747	0.1800	16.37

Table C.14. Pin Fin Coupon C High Pressure Ratio Room Temperature Sand Results

High PR (> 1.1)				
Sand [g]	**SR [s]**	**PR**	**FP**	**RFP (%)**
1.75	0.26	1.4099	0.3404	0.00
1.75	0.26	1.3573	0.3368	0.00
2.26	0.41	1.1835	0.2867	0.60
2.26	0.41	1.1724	0.2806	0.80
2.26	0.41	1.1676	0.2760	1.52
2.63	0.40	1.4212	0.3429	0.00
2.63	0.40	1.4393	0.3415	0.00
3.50	0.53	1.4373	0.3427	0.00

Table C.15. Pin Fin Coupon C Heated Sand Results

PR	RFP (%)
1.030	18.4
1.038	15.5
1.055	14.7
1.084	13.6
1.024	17.5
1.037	15.7
1.043	15.5
1.052	15.4
1.062	14.0
1.079	14.2

Appendix D: Air Compressibility Effect on Friction Factor

Nomenclature

a	speed of sound	
D	pin diameter	
D_H	hydraulic diameter:	$D_H = \frac{2(W \cdot H)}{(W+H)}$
f	friction factor:	$f = \frac{\Delta P}{0.5(\rho_i \cdot V_i^2)} \frac{D_H}{L}$
H	channel height	
L	channel length	
ΔP	pressure difference	
Re	Reynolds number:	$Re = \frac{\rho \cdot V \cdot D_H}{\mu}$
Re_D	Reynolds number:	$Re_D = \frac{\rho \cdot V_m \cdot D}{\mu}$
V	velocity	
V_m	velocity between spanwise pins	
W	channel width	

Greek

ρ	density
μ	dynamic viscosity

Subscript

i	inlet
o	outlet

While trying to baseline the pressure drop test stand against the Blasius fully turbulent, smooth wall friction factor correlation, as seen in Equation D.1 [1], the effect of air compressibility was measured at the high Reynolds numbers. When the Mach number reached the onset of the compressibility regime, the friction factor began to deviate from the Blasius correlation and rise quickly. To offset this, higher pressure compressed air of 620 kPa was used instead of the initial 450 kPa. This allowed testing over the same Reynolds number range, but at a lower air velocity. As seen in Figure D.1, this high pressure air caused the air compressibility effects to be diminished, as the measured friction factor then matched the Blasius correlation over the range of Reynolds numbers tested.

$$f = 0.316 \cdot Re^{-0.25} \quad \text{(E.1)}$$

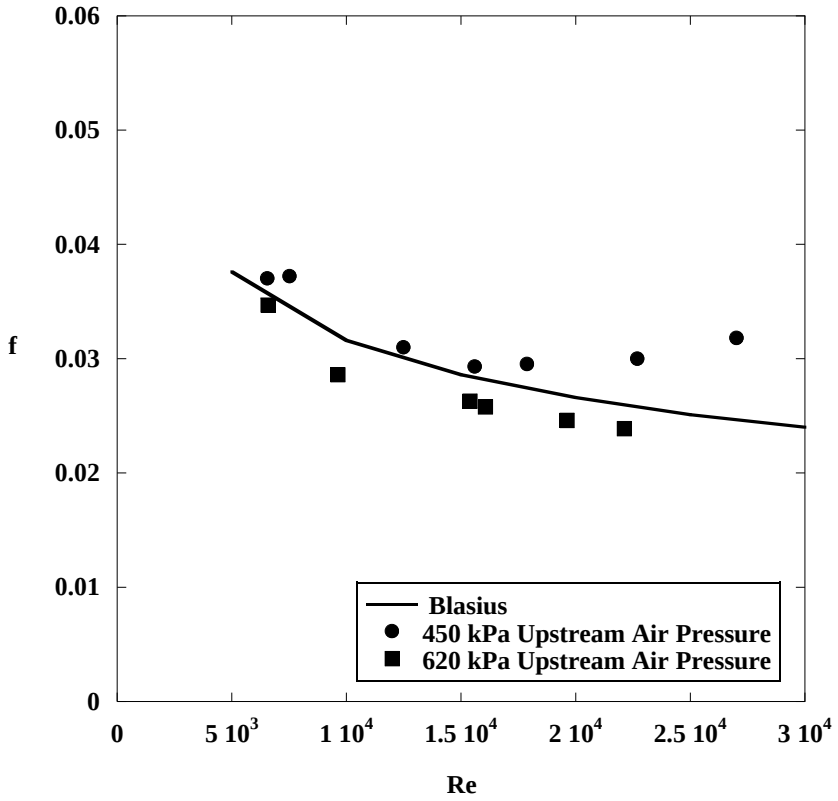

Figure D.1. Friction factor results for baseline smooth coupon with two upstream chamber pressures.

The Mach numbers through the channel for the baseline smooth coupon and the four pin fin array coupons are shown below in Figures D.2 and D.3. Figure D.2 shows the Mach number reduction at a fixed Reynolds number by increasing the upstream chamber air pressure as described before for the baseline smooth coupon. Figure D.3 shows the Mach numbers for the four pin fin coupons only at the higher upstream air pressure. Above a Reynolds number of approximately 1.5×10^4, air compressibility effects were again starting to be measured on the pin fin array friction factor as the friction factor started to level off and then rise for increasing Reynolds numbers. The compressibility effect onset happened at lower Reynolds numbers for the pin fin arrays since the channel characteristic velocity was based off the velocity between the spanwise pins instead of the average duct velocity.

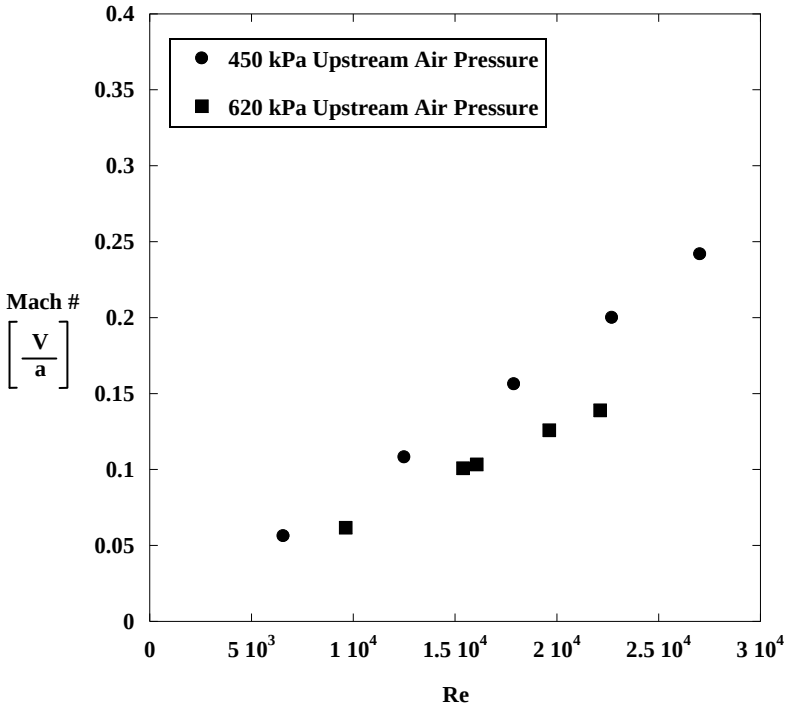

Figure D.2. Mach number results as a function of Reynolds number for the baseline smooth coupon with two upstream chamber pressures.

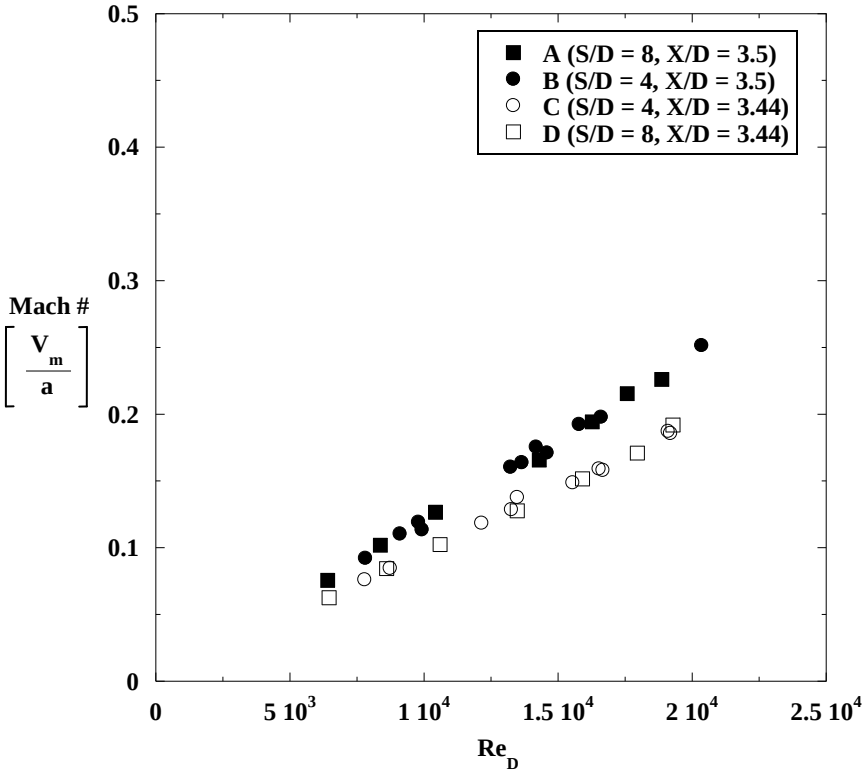

Figure D.3. Mach number results as a function of Reynolds number for the four clean coupons at an upstream pressure of 620 kPa.

References

[1] White, F.M., 1994, Fluid Mechanics (3rd ed.). New York: McGraw-Hill College, pp. 313-340.